Alchemical Enhanced Sampling with Optimized Phase Space Overlap

Shi Zhang, Timothy J. Giese, Tai-Sung Lee, and Darrin M. York*

Read Online

ACCESS | 📊 Metrics & More | 📖 Article Recommendations | 🆂🅸 Supporting Information

ABSTRACT: An alchemical enhanced sampling (ACES) method has recently been introduced to facilitate importance sampling in free energy simulations. The method achieves enhanced sampling from Hamiltonian replica exchange within a dual topology framework while utilizing new smoothstep softcore potentials. A common sampling problem encountered in lead optimization is the functionalization of aromatic rings that exhibit distinct conformational preferences when interacting with the protein. It is difficult to converge the distribution of ring conformations due to the long time scale of ring flipping events; however, the ACES method addresses this issue by modeling the *syn* and *anti* ring conformations within a dual topology. ACES thereby samples the conformer distributions by alchemically tunneling between states, as opposed to traversing a physical pathway with a high rotational barrier. We demonstrate the use of ACES to overcome conformational sampling issues involving ring flipping in ML300-derived noncovalent inhibitors of SARS-CoV-2 Main Protease (M^{pro}). The demonstrations explore how the use of replica exchange and the choice of softcore selection affects the convergence of the ring conformation distributions. Furthermore, we examine how the accuracy of the calculated free energies is affected by the degree of phase space overlap (PSO) between adjacent states (i.e., between neighboring λ-windows) and the Hamiltonian replica exchange acceptance ratios. Both of these factors are sensitive to the spacing between the intermediate states. We introduce a new method for choosing a schedule of λ values. The method analyzes short "burn-in" simulations to construct a 2D map of the nonlocal PSO. The schedule is obtained by optimizing an alchemical pathway on the 2D map that equalizes the PSO between the λ intervals. The optimized phase space overlap λ-spacing method (Opt-PSO) leads to more numerous end-to-end single passes and round trips due to the correlation between PSO and Hamiltonian replica exchange acceptance ratios. The improved exchange statistics enhance the efficiency of ACES method. The method has been implemented into the `FE-ToolKit` software package, which is freely available.
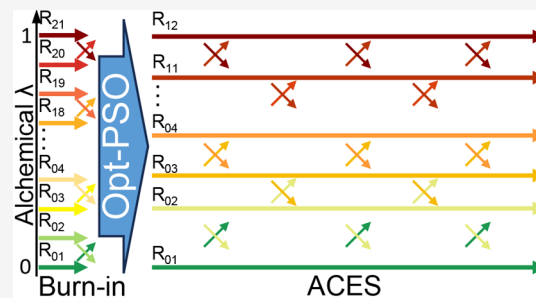
1. INTRODUCTION

Alchemical free energy (AFE) simulations[1−10] play an important role in computer-aided drug discovery.[11−13] They are used in lead refinement to predict target binding affinity and selectivity in order to prioritize proposed compound synthesis and testing. AFE simulations use an artificial "alchemical" coordinate (referred to as "λ") to transform one ligand into another in a relative binding free energy (RBFE) calculation.[1,4] Alternatively, absolute binding free energy calculations[14,15] "annihilate" the ligand by transforming it into a noninteracting "dummy" state.[16−18] The reliability of AFE simulations depends critically on the ability to robustly sample the important regions of phase space along the entire alchemical pathway. Although the free energy is a state function, the convergence of a free energy estimate is sensitive to the size of the perturbation, the form of the λ-dependent potential energy function, and the methods used to sample the path.

A vast literature of methods has evolved that seek to improve the design of alchemical transformation pathways[19−30] and their sampling.[25,31−40] For more extensive discussion, we refer the reader to several excellent reviews.[1,4,8,41−45] Recently, an

AlChemically Enhanced Sampling (ACES) method[46] has been introduced that enables focused enhanced sampling of select regions involving the ligand undergoing alchemical transformation and/or the nearby residues. The foundation of the method is to create an artificial noninteracting "enhanced-sampled" state that can be rigorously connected to the corresponding real state end-point through Hamiltonian replica exchange.[47−49] The enhanced sampled state is a selection of atoms (the ligand, a subset of the ligand, and/or nearby protein residues) whose intermolecular interactions with the environment are removed. Furthermore, certain intramolecular energy terms within the region are scaled (such as electrostatics, and torsion angle/1−4 Lennard-Jones terms associated with
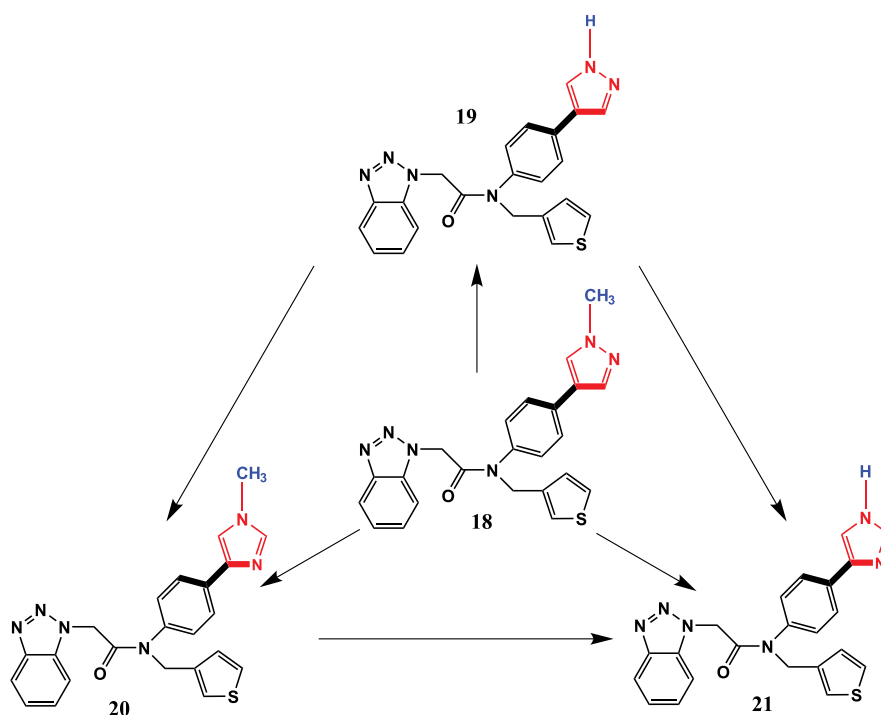
Figure 1. Thermodynamic graph showing the transformation among the four ligands[66] designated: **18**, **19**, **20**, and **21**. The torsion angle about which ring flipping occurs is emphasized in bold. The softcore region defined by the MCS/E atom mapping algorithm is highlighted in blue, and those defined by ACES is highlighted in red.

rotations about single bonds). The idea of creating an enhanced sampled state and connecting it to the desired real state endpoint with replica exchange is embraced in many other methods, including REST[50] and REST2.[51] However, a caveat for many of these approaches is that the enhanced-sampled noninteracting state may require considerable rearrangement of the environment. For example, this would occur if an entire ligand in the binding pocket of a protein were transformed into an enhanced sampled state. The elimination of the intermolecular interactions creates a void that would need to be (partially) replaced by solvent and/or accommodated by the rearrangement of the binding pocket itself (e.g., the closing of flaps) into an apo state. These conditions greatly increase the sampling requirements and the number of λ-windows connecting it to the real state.

A feature of ACES that distinguishes it from some other replica exchange methods such as REST/REST2,[50,51] is that it uses synchronous counterpoised alchemical transformations between real and enhanced sampled states to reduce the perturbation on the environment. This is achieved using a dual topology framework whereby the enhanced sampled regions of each ligand have separate coordinates—designated the softcore (SC) region—that do not interact with one another. The environment, on the other hand, interacts with a weighted average of both topologies along the alchemical dimension so as to produce the effect of a fully occupied (transforming) ligand. The separable topology is key: whereas the environment feels the effect of both ligands as a weighted average, the SC regions of the transforming ligands do not feel one another and can thus adopt different conformations. This allows enhanced sampled states to "tunnel through" barriers that would otherwise be encountered in the real state. The general idea of exploiting a dual-topology framework with alchemical enhanced sampling has been used in similar contexts[31,48,52−56] and it remains an active area of research.[46,57,58] It is in the details of how these

methods are achieved and implemented into performance software that distinguishes them as evolving practical tools for drug discovery. Other alternative strategies have also emerged that have shown considerable promise, including enveloping distribution sampling[55−57,59,60] and the alchemical transfer method.[9,13,61,62]

The ACES method further leverages recently developed optimized alchemical pathways and smoothstep softcore potentials[63] to create stable intermediate states and free energy estimates. Even with these advanced features, the selection of a larger SC region does come with an increased sampling requirement, both at the enhanced-sampled end state and along the λ-dimension. A question thus arises as to how one may best choose the SC region in the ACES method to achieve optimal importance sampling while minimizing the computational requirement. This choice will undoubtedly be problem-specific; the goal in the present work is to study one commonly occurring scenario involving ring-flipping in ligands to establish recommended best practices for the ACES SC region in this use case. We further develop a new technique for determining optimal phase space overlap λ-spacing (Opt-PSO) to improve the replica-exchange acceptance ratios and sampling efficiency with ACES.

1.1. Ring Flipping in SARS-CoV-2 Main Protease Inhibitors. Many drug-like compounds contain a rotatable ring connected to the molecular scaffold by a single bond. In the simplest case of a ring possessing C_{2v} symmetry (with one mirror plane in the plane of the ring and the second mirror plane containing the single bond and bisecting the ring), a rotation about the single bond by 180 deg produces an identical structure. For rings containing asymmetric functional groups, this rotation can reposition the functional groups while preserving the overall space filling requirements of the ring. This transition becomes important in alchemical free energy

simulations when a functional group on the ring is transformed from a state that makes a favorable interaction with the protein to one that is strained or sterically hindered. In this case, the unfavorable interaction can be alleviated by flipping of the ring. The time scale required to observe ring flipping events in a protein environment can be well beyond the sampling performed in routine molecular dynamics (MD) and alchemical free energy simulations.

An example of such a situation occurs with the SARS-CoV-2 main protease (M^{pro}). ML300[64] is a noncovalent inhibitor originally discovered to target SARS-CoV-1 M^{pro}. It has gained much interest due to the overall 96% sequence identity and 100% identity in the active site between SARS-CoV-1 and SARS-CoV-2 M^{pro} proteins.[65] A series of ML-300 derived compounds were synthesized and tested against SARS-CoV-2 M^{pro}, among which ligand **19** (PDB: 7LMD) and **21** (PDB: 7LMF) showed promising IC_{50}.[66] The high binding affinities between the ligands and SARS-CoV-2 M^{pro} (0.106 μ M for **19** and 0.063 μ M for **21**) are attributed to the potential for multiple H-bonding interactions from heterocyclic azole nitrogens. There are prospective H-bonds with both the hydroxyl side chain of Thr25 and the backbone carbonyl of Cys44 in the crystal structure. However, the binding affinities were drastically diminished in the N-methyl analogues **18** and **20**, due to the replacement of the $-H$ with $-CH_3$ (Figure 1). This underscores the importance of the presence and nature of a H-bond donor in the $P2_c$ group.[66] The steric hindrance presented by the methyl group leads to poor inhibition against the target protein. Such hindrance can be alleviated by the flipping of the heterocyclic azole ring by roughly 180 deg. We use this as an illustrative example to show how ACES can be used to robustly sample ring flipping events that occur in RBFE calculations, which leads to more precise free energy estimates.

The remainder of the paper is organized as follows. The Methods section begins with a theoretical description of ACES and the Opt-PSO method for optimizing the λ schedule. Technical details of the implementation, as well as computational details for the simulations, are provided. The Results and Discussion section presents a series of demonstrations using ACES. The first demonstration compares the ability of ACES and traditional MD to sample ring conformation distribution functions. The second demonstration applies ACES in the context of RBFE calculations involving a dense thermodynamic graph containing closed cycles. The third demonstration uses the Opt-PSO method (optimized λ-spacing) to improve ACES performance. The Conclusion section summarizes the main points of the paper and identifies areas of future work.

2. METHODS

2.1. Alchemical Enhanced Sampling Method.
We recently introduced and implemented[46] the ACES method in AMBER which integrates the following novel features:

- Localized enhanced sampling states created through the tuning of intra- and intermolecular energy terms; i.e., noninteracting "dummy" states,[18] and the modification of internal energy terms to eliminate kinetic traps;

- Robust alchemical transformation pathways that connect real and enhanced sampled states using new smoothstep softcore potentials, nonlinear Hamiltonian mixing, and flexible λ-scheduling capabilities;[63]

- An efficient HREMD framework that maintains equilibrium between λ-windows connecting the real and

localized enhanced sampled states within a dual-topology approach.

The ACES approach[46] has advantages due to its dual-topology nature[31] that allow it to overcome local "hot-spot" problems encountered with REST/REST2.[67] As the ACES region of the λ = 0 real state (e.g., Ligand 1) is "annihilated",[18] the ACES region of the λ = 1 real state (e.g., Ligand 2) is "created". Unlike REST2, the concerted "counter-diffusion" of alchemical states produces minimal rearrangement of the environment along the λ path. Furthermore, the computational overhead of the method is negligible relative to conventional AFE simulations with HREMD. Although ACES can be used along with REST2,[67] which does incur added computational cost, the results suggest that there is little gain beyond using ACES alone.[46] The efficiency and robustness of the ACES approach relies heavily on the HREMD framework. If the HREMD acceptance ratio is very small, then there will be too few walker end-to-end "single passes" and "round trips"[68] to adequately connect the enhanced sampled state and end-state with the correct Boltzmann distribution. A "single pass" is the traversal of a walker from the λ = 0 state to the λ = 1 state, or vice versa, through a series of exchanges between the intermediate λ-states. A "round trip" is similarly the traversal of a walker from the λ = 0 to λ = 1 states and back to the λ = 0 state. The HREMD acceptance ratio is highly correlated with the "phase space overlap" between adjacent intermediate states.[69−72] In other words, the replica exchange acceptance ratio is sensitive to the spacing between λ-windows. The next section introduces new methods for choosing a λ-schedule, for a given number of points, that optimizes the phase space overlap, or alternatively the Kullback−Leibler divergence of replica exchange acceptance ratio, and improves the HREMD and ACES efficiency.

2.2. Optimized λ-Scheduling Methods.
This section describes new methods for determining optimal spacing λ schedule based on short "burn-in" ACES simulations by creation of a 2D map in λ space. The 2D map $O(\lambda, \lambda')$ represents a predictive measure of the phase space overlap involving the intervals defined by λ and λ'. The goal of the procedure is, for a desired number of λ windows, N_λ, determine the set of λ_i values ($i = 1, ... N_\lambda$) that span the range $[0, 1]$ such that the phase space overlap index is predicted to be uniform for all adjacent intervals (λ_i, λ_{i+1}) and the lowest value maximized. The rationale is that this schedule should provide improved HREMD and ACES efficiency, and more robust free energy predictions. The methods differ by the specific index related to phase space overlap that is used to create the 2D map. These include the phase space overlap[69−72] (PSO), Kullback−Leibler divergence[73] (KL) and replica exchange acceptance ratio[68] (AR), and are described in more detail below.

2.2.1. Optimized Phase Space Overlap λ-Scheduling (Opt-PSO). Let $U(\mathbf{r}; \lambda)$ denote the potential energy of a λ-dependent potential energy function evaluated with the $3N$ array of atomic coordinates $\mathbf{r}$. Simulation of $U(\mathbf{r}; \lambda_k)$ produces an ensemble of M_k structures $\{\mathbf{r}_{k1}, \mathbf{r}_{k2}, ..., \mathbf{r}_{k,M-1}, \mathbf{r}_{k,M_k}\}$, where $\mathbf{r}_{kn}$ denotes sample n from ensemble k. If equilibrium sampling is performed, then the distribution of energy differences $\Delta U_{ij}(\mathbf{r}_{kn}) = U(\mathbf{r}_{kn}; \lambda_i) - U(\mathbf{r}_{kn}; \lambda_j)$ will often be well-approximated by a normal distribution (eq 1) parametrized by the mean $\langle \Delta U_{ij} \rangle_k$ and standard deviation σ_{ijk}.

$$\rho_k(\Delta U_{ij}) = \left(\frac{1}{2\pi\sigma_{ijk}^2}\right)^{1/2} e^{-(\Delta U_{ij}-\langle \Delta U_{ij}\rangle_k)^2/2\sigma_{ijk}^2}$$

(1)

$$\langle \Delta U_{ij} \rangle_k = \frac{1}{M_k} \sum_{n=1}^{M_k} \Delta U_{ij}(\mathbf{r}_{kn}) \tag{2}$$

$$\sigma_{ijk} = \sqrt{\sum_{n=1}^{M_k} \frac{(\Delta U_{ij}(\mathbf{r}_{kn}) - \langle \Delta U_{ij} \rangle_k)^2}{M_k - 1}} \tag{3}$$

The overlap of the normal distributions observed from simulation of states i and j shall be denoted S_{ij}^{ij} (a special case of eq 4) which is used to define an "overlap index" (eq 5) that measures the similarly between the ensembles.

$$S_{ij}^{kl} = \int \rho_i(\Delta U_{kl}) \rho_j(\Delta U_{kl}) \, d\Delta U_{kl} \tag{4}$$

$$O_{ij} = S_{ij}^{ij} / \max(S_{ii}^{ij}, S_{jj}^{ij}) \tag{5}$$

Specifically, the index is the overlap of the distributions using a normalization convention that ensures $0 \leq O_{ij} \leq 1$ for all ij, and the self-overlap index is guaranteed to be unity, $O_{ii} \equiv 1$. The overlap index is a continuous function of the normal distribution mean and standard deviation values; however, the derivative of overlap index with respect to a standard deviation is discontinuous when the normal distributions share the same standard deviation. The standard deviations are not free parameters in the Opt-PSO method; their values are determined from the observations made from short "burn-in" simulations, described below.

If one performed brief simulations with a schedule consisting of N_λ states, then the analysis of these ensembles with eq 5 produces a $N_\lambda \times N_\lambda$ symmetric matrix of overlap indexes, whose diagonal elements are unity. One can approximate the overlap between any pair of states by concocting a continuous function $O(\lambda, \lambda')$ that is parametrized to reproduce $O(\lambda_i, \lambda_j) = O_{ij}$ for all $N_\lambda \times N_\lambda$ observations while also obeying the secondary property $O(\lambda, \lambda) = 1$ for all continuous values $\lambda \in [0, 1]$. To enforce this second property, we make use of a coordinate transformation (eqs 6–7).

$$u(\lambda, \lambda') = (\lambda - \lambda') / \sqrt{2} \tag{6}$$

$$v(\lambda, \lambda') = (\lambda + \lambda') / \sqrt{2} \tag{7}$$

If one visualizes O_{ij} as a two-dimensional regular grid of values, then the u- and v-coordinates correspond to the distances orthogonal and parallel to the diagonal, respectively. An interpolating function that enforces the second property can then be written.

$$O(\lambda, \lambda') = e^{-z(u(\lambda, \lambda'), v(\lambda, \lambda')) u(\lambda, \lambda')^2} \tag{8}$$

We use multiquadric radial basis functions (RBF), $\varphi(r) = \sqrt{1 + (\epsilon r)^2}$, to model the exponent, $z(u, v)$, where $\epsilon = 100$ is "shape parameter" and r is a Euclidean distance in the RBF coordinate space.

$$z(u, v) = \sum_{ij} w_{ij} \varphi\left(\sqrt{(u - u_{ij})^2 + (v - v_{ij})^2}\right) \tag{9}$$

The u_{ij} and v_{ij} values are the locations of the observations, and the values of $z(u, v)$ which cause $O(\lambda_i, \lambda_j) = O_{ij}$ are given by z_{ij}.

$$u_{ij} = u(\lambda_i, \lambda_j) \tag{10}$$

$$v_{ij} = v(\lambda_i, \lambda_j) \tag{11}$$

$$z_{ij} = -\ln(O_{ij}) / u_{ij}^2 \tag{12}$$

The RBF is parametrized to reproduce the z_{ij} values by solving the following set of simultaneous equations for the weights w_{ij}.

$$\sum_{kl} A_{(ij),(kl)} w_{kl} = z_{ij} \tag{13}$$

Infinitely smooth RBFs, such as multiquadrics, are strictly positive definite functions; therefore, $\mathbf{A}$ is invertible and a unique solution for the weights can be found.

$$A_{(ij),(kl)} = \varphi\left(\sqrt{(u_{ij} - u_{kl})^2 + (v_{ij} - v_{kl})^2}\right) \tag{14}$$

The $O(\lambda, \lambda')$ interpolating function is used to predict a λ-schedule with improved ensemble overlaps. Specifically, we fix the values $\lambda_1 = 0$ and $\lambda_{N_\lambda} = 1$ and adjust the remaining $N_\lambda - 2$ values in a nonlinear optimization procedure to minimize the objective function shown in eq 15.

$$\chi^2(\lambda) = \frac{1}{N_\lambda - 1} \sum_{i=1}^{N_\lambda - 1} [O(\lambda_i, \lambda_{i+1}) - \langle O(\lambda) \rangle]^2 \tag{15}$$

The objective function is the variance between the $N_\lambda - 1$ nearest-neighbor overlaps, where $\langle O(\lambda) \rangle$ is the mean nearest-neighbor overlap.

$$\langle O(\lambda) \rangle = \frac{1}{N_\lambda - 1} \sum_{i=1}^{N_\lambda - 1} O(\lambda_i, \lambda_{i+1}) \tag{16}$$

We optimized eq 15 using the low-storage Broyden-Fletcher-Goldfarb-Shanno algorithm[74] implemented in the SciPy software.[75] The derivatives $\partial \chi^2 / \partial \lambda_i$ were approximated from a central finite difference using a displacement of 5×10^{-5}.

2.2.2. Optimized Kullback−Leibler Divergence λ-Scheduling (Opt-KL). The Kullback−Leibler (KL) divergence is another property used to quantify the similarity between distributions.[73] Specifically, $D(\rho_i \| \rho_j)$ is a statistical measure of how ρ_i differs from ρ_j.

$$D(\rho_i \| \rho_j) = \int_{-\infty}^{\infty} \rho_i(\Delta U_{ij}) \ln\left(\frac{\rho_i(\Delta U_{ij})}{\rho_j(\Delta U_{ij})}\right) d\Delta U_{ij} \tag{17}$$

When applied to normal distributions, the integral simplifies to eq 18.

$$D(\rho_i \| \rho_j) = \ln \frac{\sigma_{ijj}}{\sigma_{iji}} + \frac{\sigma_{iji}^2 + (\langle \Delta U_{ij} \rangle_i - \langle \Delta U_{ij} \rangle_j)^2}{2\sigma_{ijj}^2} - \frac{1}{2} \tag{18}$$

Kullback−Leibler similarly developed a symmetric form of the measure, which we denote as D_{SKL}.[73]

$$D_{\mathrm{SKL}}(\rho_i \| \rho_j) = \frac{1}{2}(D(\rho_i \| \rho_j) + D(\rho_j \| \rho_i)) \tag{19}$$

D_{SKL} is 0 when the two distributions are the same, and it approaches $+\infty$ as their differences increase. Eq 20 exponentiates D_{SKL} to place the domain in the range $(0, 1)$, arriving at an alternate definition of the overlap index, which we call the "KL index".

$$O_{ij} = e^{-D_{\mathrm{SKL}}(\rho_i \| \rho_j)} \tag{20}$$

The construction of a continuous, nonlocal function of KL index and its optimization to determine a λ-schedule is analogous to eqs 8−15.

2.2.3. Optimized Replica Exchange Acceptance Ratio λ-Scheduling (Opt-AR). The Opt-AR method makes a direct estimate of the replica exchange acceptance probability ratio to optimize a λ-schedule. The probability of exchange between states i and j at time step n is calculated from the Metropolis criterion at constant temperature.

$$p_{ijn} = \min\left(1, \, e^{-\beta[\{U(\mathbf{r}_{jn};\lambda_i) + U(\mathbf{r}_{in};\lambda_j)\} - \{U(\mathbf{r}_{in};\lambda_i) + U(\mathbf{r}_{jn};\lambda_j)\}]}\right)$$

$$= \min\left(1, \, \frac{e^{-\beta\Delta U_{ij}(\mathbf{r}_{jn})}}{e^{-\beta\Delta U_{ij}(\mathbf{r}_{in})}}\right) \tag{21}$$

The Opt-AR method replaces the overlap index with a "AR index" defined by the average exchange probability.

$$O_{ij} = \frac{1}{\min(M_i, M_j)} \sum_{n=1}^{\min(M_i, M_j)} p_{ijn} \tag{22}$$

Preliminary examination of the AR indexes suggested to us that the values are modeled slightly better with an exponential (eq 23) rather than a Gaussian (eq 8); however, the differences between the model functions are quite small because they are both parametrized to reproduce the observed AR index values.

$$O(\lambda, \lambda') = e^{-z(u(\lambda,\lambda'),v(\lambda,\lambda'))|u(\lambda,\lambda')|} \tag{23}$$

The exponent is a continuous function calculated from a RBF (eq 9) whose weights are parametrized (eq 13) to match the discrete exponent values (eq 24) needed to reproduce the observed AR indexes, $O(\lambda_i, \lambda_j) = O_{ij}$.

$$z_{ij} = -\ln(O_{ij})/|u_{ij}| \tag{24}$$

The optimization of a schedule from eq 23 is analogous to eqs 15 and 16.

2.3. Computational Details. We describe the relevant molecular system setup and simulation protocols as follows. All simulations in the present work were performed with the GPU-accelerated version of pmemd, as implemented in the AMBER Drug Discovery Boost package (AMBER DD Boost).[76] This modified software patch has been fully integrated within Amber since version AMBER22.[77] Free energy analysis was performed using the FE-ToolKit[78,79] software package included in AmberTools.[80]

The systems were prepared in accord with our ProFESSA free energy workflow.[81] A few technical points of the system preparation using our workflow are discussed here. The calculation of RBFE values for a series of structurally related ligands can be viewed as a transformation network, where the nodes of the graph are the physical states and a graph edge is an alchemical transformation between two states. Technically, there are two networks corresponding to the ligand transformations performed in aqueous and protein-complexed environments. Each node of the graph is connected by one-or-more edges; therefore, to reuse the same physical state in multiple transformations, each system must be prepared in a consistent manner. That is to say, each system (for a given environment) was prepared with the exact same number of water molecules and Na^+ and Cl^- ions. Similarly, the unit cell shape was made consistent because the HREMD simulations performed with Amber in the *NPT* ensemble are restricted to

isotropic fluctuations in the unit cell volume. Upon equilibrating the physical end-states, the alchemical states along an edge are prepared using a "2-state" approach.[81] Specifically, the $\lambda = 0$ alchemical state (containing a dual-topology of the $\lambda = 0$ and $\lambda = 1$ physical states) is prepared and equilibrated using a procedure described in more detail below. The alchemical states corresponding to $0 < \lambda \leq 0.5$ are sequentially equilibrated from the previous λ alchemical state, and the remaining states are similarly equilibrated in a sequential fashion starting from the $\lambda = 1$ alchemical state. This two-state preparation has previously been found to remove bias caused by "hysteresis" in the sense there is no "forward" or "reverse" direction in the simulations.[81] A more detailed discussion of why this is important to obtain high precision has been described elsewhere.[1]

The protein and the ligand systems were modeled using the AMBER ff14SB and the GAFF2 force fields,[82] respectively, and the condensed phase environment was explicitly modeled with TIP4P/Ew waters[83] with the corresponding Joung−Cheatham Na^+ and Cl^- ion parameters.[84,85] All simulations were carried out using a 1 fs integration time step. Constant temperature simulations were performed with the Langevin thermostat using a 5 ps^{-1} collision frequency.[86] Simulations performed in the *NPT* ensemble further used the Monte Carlo barostat to maintain a pressure of 1 atm. Electrostatics were evaluated with the particle mesh Ewald (PME) method[87,88] using a 1 Å grid spacing and 10 Å real-space cutoffs. The Lennard-Jones interactions were truncated at 10 Å and a long-range tail correction was applied. SHAKE[89] constraints were applied to protein covalent bonds involving hydrogen.

2.3.1. System Preparation. We first prepared reference end-state systems containing ligands **19** and **21**, because crystal structures of these ligands bound to SARS-CoV-2 M^{pro} are available (PDB ID 7LMD and 7LMF,[66] respectively). Ligands **18** and **20** were then prepared in a consistent way based on the reference systems. Starting from the crystal structures, the tLeap program[80] was used to add missing hydrogen atoms and solvate the protein with 19136 waters to form an orthorhombic cell. A total 83 Na^+ and 75 Cl^- ions were added to counter balance the protein charge and reach an approximate physiological (extracellular) bulk concentration of 0.15 M. For the ligands in aqueous solution a similar procedure was used: the initial structures of ligands were taken from the protein complex and solvated by 4904 waters, 13 Na^+, and 13 Cl^-. The end-state systems for ligands **18** and **20** were setup in a similar fashion upon replacing the imidazole hydrogen with a methyl group (Figure 1). Special care was taken to use the same number of waters, ions, and unit cell.

2.3.2. Relative Binding Free Energy Simulation Protocols. Following the ProFESSA workflow,[81] the positions of the ions and water molecules were geometry optimized for 5000 steps using the steepest descent method while restraining the solute heavy-atom positions with a force constant of 5 kcal/mol/Å². These restraints were then released and the system was optimized for an additional 5000 steps. Equilibration was performed in the *NPT* ensemble for 500 ps while restraining the solute heavy-atom positions with a force constant of 5 kcal/mol/Å². Targeted volume MD[76] was performed on both end-states to average the box dimensions for 500 ps in order to generate the intermediate replicas with the same box shape.

The system was heated at constant volume for 500 ps to achieve a temperature of 300 K. After heating, a 500 ps equilibration in the *NPT* ensemble was performed, followed by 2 ns annealing in the *NVT* ensemble. The annealing heated the
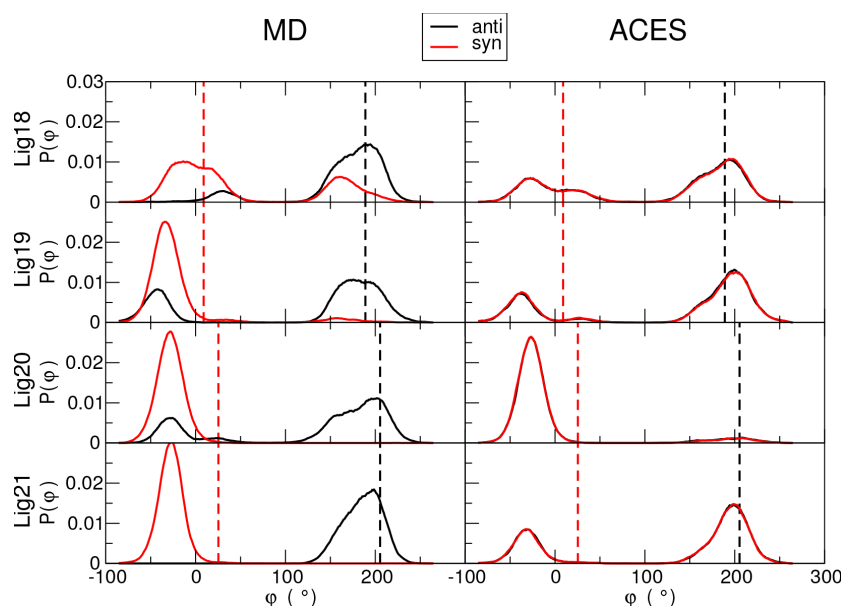
Figure 2. Distributions for the torsion, $P(\psi)$, are obtained from MD (left) and ACES (right) simulations departing independently from initial states with the torsion (ψ) taken to be the value (indicated by dashed vertical lines) obtained from the crystal structures for ligands **19** and **21** (black) and alternatively flipped by 180 deg (red). Here the ACES simulations are for "self transformations"; e.g., $18 \to 18$, $19 \to 19$, $20 \to 20$ and $21 \to 21$. All results are the average of 4 independent runs (trials).

system from 300 to 600 K in the first 50 ps, maintained a temperature of 600 K for an additional 100 ps, and then cooled the system to 300 K over a period of 50 ps. After the annealing stage, the solute heavy atom restraints were gradually reduced over a period of 1 ns in the *NPT* ensemble at 300 K and 1 atm. The unrestrained system was then equilibrated for an additional 200 ps. The above procedure was performed for the $\lambda = 0$ and $\lambda = 1$ physical states. Dual topology structures were prepared, and the alchemical states were sequentially equilibrated from $\lambda = 0$ to $\lambda = 0.5$ (and from $\lambda = 1$ to $\lambda = 0.5$). The starting configuration of each alchemical state is the equilibrated structure of the previous λ state in the sequence. Each alchemical state was minimized with 5000 steps with the steepest descent method, heated to 300 K over a period of 300 ps at constant volume, and equilibrated for an additional 2.2 ns at 300 K in the *NPT* ensemble.

The alchemical transformations were performed using the modified SSC(2) softcore potential and the one-step concerted softcore protocol.[63] The unitless parameters of the softcore potential are m = 2, n = 2, $\alpha = 0.5$, and $\beta = 1$. The implementation of the SSC(2) softcore potential in the pmemd program includes options which control the λ-dependence of the bonded terms crossing the common-core and softcore regions. Specifically, we set the option gti_add_sc = 25 which scales the energy of those torsions describing the rotation around a single-bond.[46] This scheme has been found to enhance the sampling and improve the convergence of the calculated free energy.[46] Unless otherwise stated, the transformations were performed with 21 λ windows spanning $\lambda = 0.0$ and $\lambda = 1.0$ in steps of 0.05.

We compare the enhanced sampling produced by ACES (which uses HREMD and an extended softcore region) with traditional sampling (which does not use HREMD and selects a minimal softcore region). In both cases, the alchemical transformation of the entire ligand is considered; however, the ACES softcore selection includes the whole imidazole ring (the ACES selection in Figure 1), whereas the non-ACES softcore selection is a subset of the ring determined from the Maximum

Common Substructure[90] (MCS) algorithm (the MCS/E selection in Figure 1). The production simulations were performed for 6 ns with a 1 fs time step in the *NPT* ensemble at 300 K and 1 atm. The ACES simulations attempt HREMD exchanges every 20 fs. Only the last 5 ns of each simulation was included in the analysis. Network-wide MBAR free energy analysis was performed on the thermodynamic graph shown in Figure 1 with cycle closure constraints[79] using FE-ToolKit.

2.3.3. Comparison of Torsion Angle Distributions. We compare torsion angle distributions of the imidazole ring computed from standard MD and ACES sampling to illustrate the enhanced sampling offered by ACES. These simulations are not used to estimate the RBFE between different ligands. As previously discussed, we prepared and equilibrated the SARS-CoV-2 M^{pro} system with ligands **18−21**. Each of these systems can be prepared twice: once when the imidazole ring torsion is in the *syn* conformation, and another in the *anti* conformation (these differ only by a 180° rotation of the ring). We then performed standard MD of the 4 systems in both the *syn* and *anti* conformations. The production sampling was performed for 6 ns in the *NPT* ensemble at 300 K and 1 atm using a 1 fs time step, and each simulation was repeated 4 times with different thermostat random number seeds. The imidazole torsion angle highlighted in Figure 1 was monitored during the last 5 ns of each simulation, and normalized histograms were constructed to illustrate the torsion angle probability distribution.

The simulations were repeated using the ACES method in a manner analogous to the RBFE simulations; however, the two topologies refer to the same system. The $\lambda = 0$ and $\lambda = 1$ states differ only in the initial coordinates: the $\lambda = 0$ state is the *syn* conformation and the $\lambda = 1$ state is the *anti* conformation. This is referred to as an ACES "self-transformation". The entire ligand was included in the alchemical transformation and the softcore region includes the whole imidazole ring. The two states are connected by 21 uniformly spaced λ states. The λ states were equilibrated with the "two-state approach" in a manner

analogous to the RBFE calculations. The ACES simulations were performed for 6 ns in the *NPT* ensemble at 300 K and 1 atm using a 1 fs time step, the HREMD exchanges were attempted every 20 fs, and the simulations were performed 4 times with different thermostat random number seeds. Two sets of imidazole torsion angle distribution functions were constructed from the last 5 ns of the $\lambda = 0$ and $\lambda = 1$ states, respectively.

3. RESULTS AND DISCUSSION

3.1. Improved Sampling of Ring Conformations with ACES. In this section, we demonstrate that ACES enhances the sampling of ring conformations relative to conventional MD simulation for the set of bound SARS-CoV-2 M^{pro} ligands illustrated in Figure 1. This demonstration is not in the context of an AFE simulation used to calculate RBFE values. Rather, we use ACES in a "self-to-self" transformation whereby a bound ligand is effectively transformed into the same ligand. In this scenario, there are two copies of the ACES region that are being simulated, and these copies do not directly interact with one another. At $\lambda = 0$, one of those copies represents the real state of the ligand, whereas the other copy is in a noninteracting dummy state. In traversing the λ-dimension from 0 to 1, the first copy is transformed from a real state into a noninteracting dummy state at $\lambda = 1$, whereas the second copy is transformed from a noninteracting dummy state into a real state. At each point along the path, the environment feels the λ-dependent weighted sum of the two transforming regions. This results in a minimal perturbation to the environment along the λ-dimension; therefore, it requires a modest amount of sampling in comparison to a larger perturbation.

An advantage of ACES resides in its ability to focus the enhanced sampling on specific degrees of freedom of interest. Although conventional MD simulations are commonly used in protein–ligand binding systems, they are often inefficient at describing equilibrium distributions between multiple thermally accessible states. In the present example, the focus is on ring-flipping conformational events that occur by torsion rotation about the single bond connecting the imidazole ring and the molecular scaffold. We examine the distribution of angles of the torsion highlighted in bold in Figure 1.

Figure 2 compares the ligand torsion angle distribution using conventional MD (left) and ACES (right) simulations, departing from the *syn* and *anti* conformations. The MD simulations for each ligand show starkly different torsion angle distributions depending on the starting point (indicated by the vertical dashed lines). The distributions clearly indicate that the populations of the conformational states are biased by their initial conditions on the time scale of the MD simulations. Departing from the *anti* conformation, the peaks remain more pronounced for the *anti* state, whereas the reverse is true when departing from the *syn* conformation. In extreme cases, such as for ligand **21**, the simulations remain trapped in the initial local conformational state and are not observed to make any transitions.

The ACES simulations, on the other hand, show torsion angle distributions that are virtually indistinguishable regardless of starting conformation. All 4 ligands produce converged populations of the *syn* and *anti* states. Ligand **20** was the only ligand that predominantly prefers one conformational state (the *syn* state). Nonetheless, unlike the MD results, ACES converges to the same distribution when departing from either an initial *syn* or *anti* conformation. In the case of ligand **21**, whereas the MD was trapped in an initial conformation and no transitions were

observed, ACES produces a converged distribution independent of starting conformation.

Table 1 compares the population *syn/anti* conformational states of the ring derived from conventional MD and ACES

Table 1. Ring-Flipping Torsion Angle Distributions from ACES Enhanced Sampling and Conventional MD^{a}

Ligand	Init. Conf.	MD		ACES	
		P_{syn}/P_{anti}	Err	P_{syn}/P_{anti}	Err
18	(*syn*)	0.69/0.31	0.32	0.38/0.62	0.00
18	(*anti*)	0.11/0.89	0.27	0.37/0.63	0.00
19	(*syn*)	0.95/0.05	0.63	0.32/0.68	0.01
19	(*anti*)	0.29/0.71	0.02	0.30/0.70	0.01
20	(*syn*)	1.00/0.00	0.08	0.93/0.07	0.00
20	(*anti*)	0.26/0.74	0.67	0.92/0.08	0.00
21	(*syn*)	1.00/0.00	0.68	0.32/0.68	0.00
21	(*anti*)	0.00/1.00	0.32	0.32/0.68	0.00
maE			0.37		0.00
rmsE			0.45		0.01

$^{a}P_{syn}$ is the probability of observing the ring torsion angle ψ in the range $[-90, 90]$. P_{anti} is the probability of finding it in the range $[90, 270]$. The probabilities are averages over 4 independent trials. "Init." refers to the initial condition of the ring when the simulation began. The initial *anti* conformations were taken from the crystallographic values within PDB ID 7LMD ($-170.0°$ for ligand **18** and **19**) and PDB ID 7LMF ($-174.6°$ for ligand **20** and **21**). The initial *syn* conformations were defined by adding 180° to the corresponding *anti* values. The absolute error (Err) is shown with respect to the average *syn/anti* values from the self-ACES simulations: ligand **18** (0.38/0.62), ligand **19** (0.31/0.69), ligand **20** (0.92/0.08) and ligand **21** (0.32/0.68).

simulations departing from different initial conformations. The results are compared to reference values determined from the average of 4 independent trials of ACES self-transformation simulations, where the two end-states started from different initial conformations. The population errors for MD results are large: half of the values are over 30% error, and 3 out of 8 values are over 60% error. The population errors for ACES are all below 2%. This demonstrates the robustness of the ACES method for sampling conformational states arising from ring-flipping events for this set of ligands.

3.2. Application of ACES to the Calculation of Relative Binding Free Energies. In this section, we apply the ACES method to the calculation of RBFE values for the ligands illustrated in Figure 1. Recall that the ACES method involves the selection of an enhanced sampling region (which is transformed into a noninteracting dummy state using a smoothstep softcore), and it uses HREMD to rigorously connect the enhanced sampling dummy state with the real state. We compare the ACES results to two other approaches: the first alternative does not use HREMD, and the second alternative uses a smaller softcore region. The goal is to decouple these two elements and analyze them separately.

In the first approach, designated "no RE", we select the same softcore region as in the ACES approach (shown in Figure 1), but Hamiltonian replica exchange is not employed. In the second approach, designated "MCS/E", we use HREMD but the softcore region was chosen from the extended maximum common substructure (MCS/E) "atom-mapping" procedure.[81] Traditional AFE simulations often use a minimal softcore region to reduce the alchemical perturbation. In contrast, the ACES approach strategically selects a larger softcore region to enhance
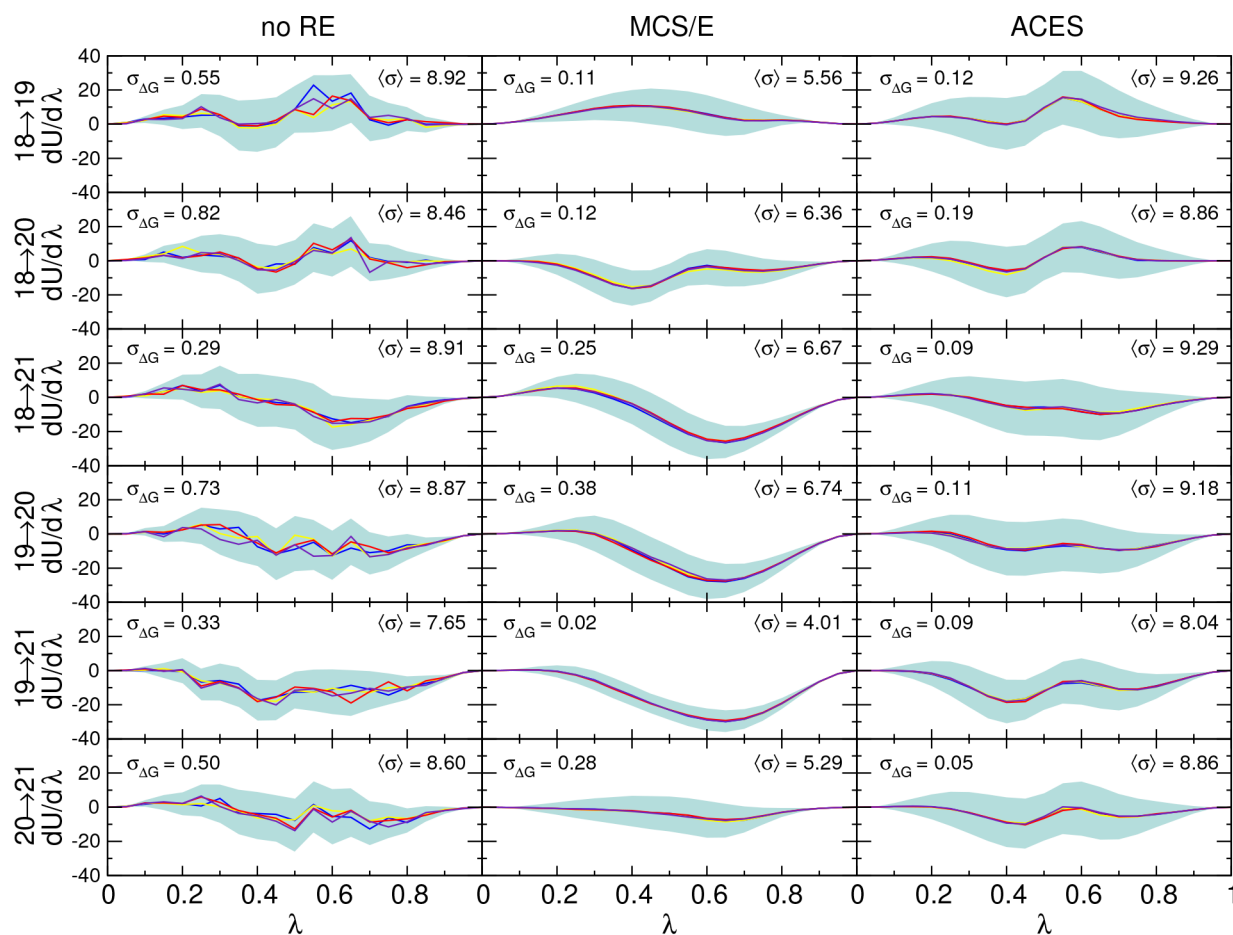
Figure 3. Profiles of $\langle dU/d\lambda \rangle_\lambda$ for the ligand transformations performed in the protein environment. Each transformation was repeated with 4 sets of simulations. The 4 solid lines are the $\langle dU/d\lambda \rangle_\lambda$ averages from each of the 4 trials. The shaded region is the standard deviation of $\langle dU/d\lambda \rangle_\lambda$ calculated from the aggregate sampling, and $\langle \sigma \rangle$ is the mean value of the standard deviation. A free energy is calculated for each trial by integrating the corresponding $\langle dU/d\lambda \rangle_\lambda$ profile with trapezoidal-rule integration. $\sigma_{\Delta G}$ is the standard deviation of the 4 free energy estimates.

sampling. In the present work, the entire ring up-to the first rotatable bond connecting it to the common core is selected as the softcore region. As was shown in the previous section, this selection enables ACES to sample multiple accessible conformational states.

Figures 3 and 4 illustrate the $\langle \partial U/\partial \lambda \rangle_\lambda$ profiles obtained from the RBFE simulations performed in the protein and aqueous environments, respectively, using the "no RE", "MCS/E" and "ACES" approaches. Each set of simulations was performed 4 times, and the shaded region is the standard deviation of $\langle \partial U/\partial \lambda \rangle_\lambda$ obtained from the aggregate sampling. The $\langle \sigma \rangle$ value is the mean value of the $\langle \partial U/\partial \lambda \rangle_\lambda$ standard deviation (averaged of the λ-states). Integration of each trial's $\langle \partial U/\partial \lambda \rangle_\lambda$ profile yields 4 estimates of the free energy change, and $\sigma_{\Delta G}$ is the standard deviation of the 4 estimates. All of the profiles appearing in Figures 3 and 4 vary smoothly; they do not display sudden jumps analogous to a first-order phase transition. The "no RE" curves exhibit larger noise between independent *lambda* windows and trials. The MCS/E method produces the smallest σ values in the protein environment. The "no RE" and "ACES" simulations yield larger σ values, and they are similar to each other. These observations are likely a consequence of the softcore region's size. The $\sigma_{\Delta G}$ values range from 0.29 to 0.82 kcal/mol (no RE), 0.02–0.38 kcal/mol (MCS/E) and 0.05–0.19 kcal/mol (ACES) in the protein environment. The average $\sigma_{\Delta G}$ value in

the protein environment is largest when replica exchange is not used (0.53 kcal/mol). In comparison, the average $\sigma_{\Delta G}$ values of MCS/E and ACES are 0.19 and 0.11 kcal/mol, respectively. The $\langle \sigma \rangle$ values range from 7.7 to 8.9 kcal/mol (no RE), 4.0–6.7 kcal/mol (MCS/E) and 8.0–9.3 kcal/mol (ACES) in the protein environment. The $\langle dU/d\lambda \rangle_\lambda$ fluctuations are largest for "no RE" and ACES due to the larger softcore region. Despite these larger fluctuations, the ACES $\langle dU/d\lambda \rangle_\lambda$ profiles produced from independent trials are remarkably similar, and the standard deviation of the free energy estimates between independent trials, $\sigma_{\Delta G}$, are comparable to (slightly smaller than) the corresponding MCS/E values. This result is likely due to the slightly more consistent ensembles generated from independent trials using ACES as opposed to MCS/E. The simulations performed in the aqueous environment display similar trends; however, the differences are less pronounced.

These results suggest that the use of HREMD is important, especially when considering a larger softcore region, to reduce the variance in the free energy estimate between independent trials. The MCS/E and ACES $\sigma_{\Delta G}$ values are often similar; however, for **18 → 21, 19 → 20**, and **20 → 21** the MCS/E values (0.25, 0.38, and 0.28 kcal/mol) are anomalously larger than the ACES values (0.09, 0.11, and 0.05 kcal/mol). In these cases, independent MCS/E runs get trapped in local conformational states. The inadequate conformational sampling leads to larger
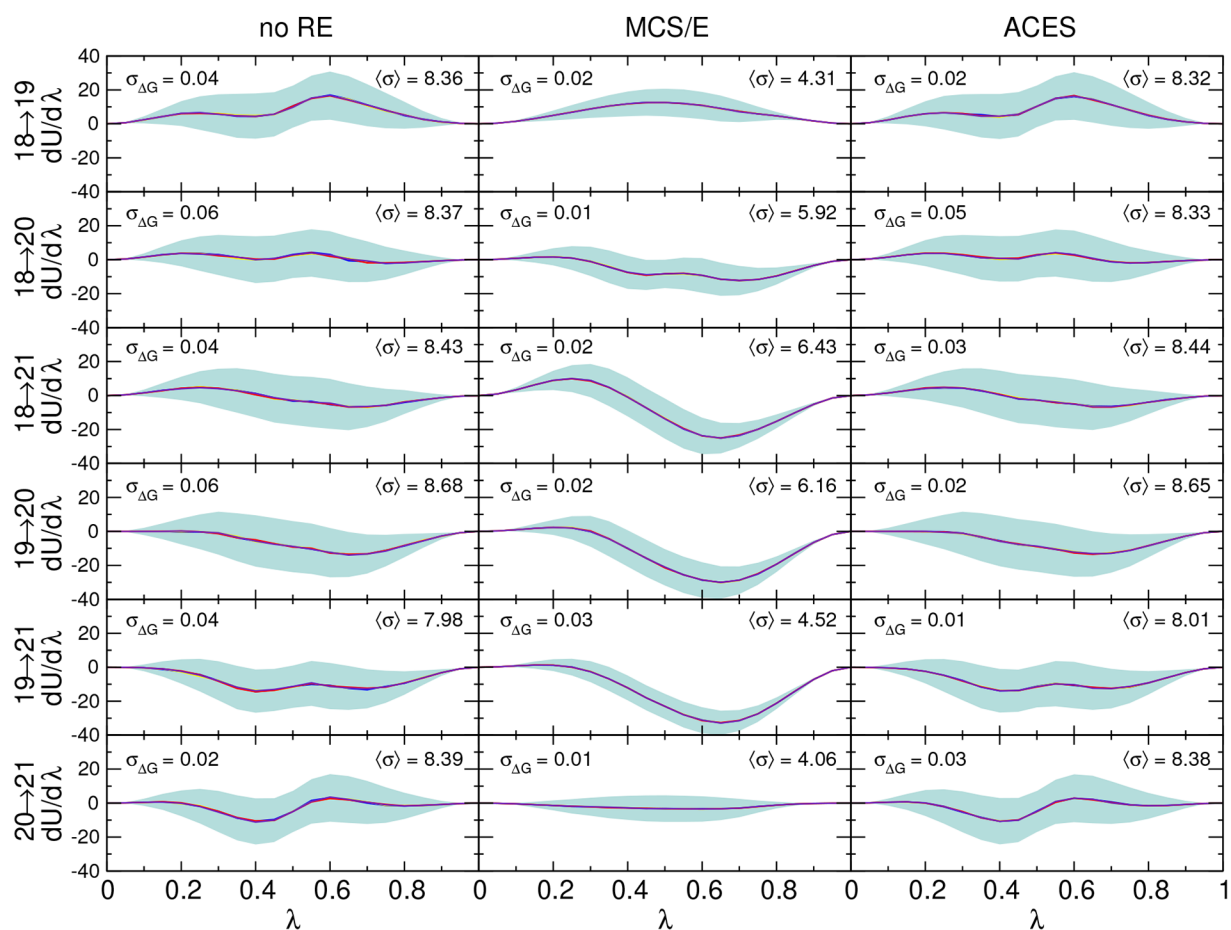
Figure 4. Profiles of $\langle dU/d\lambda \rangle_\lambda$ for the ligand transformations performed in the aqueous environment. Each transformation was repeated with 4 sets of simulations. The 4 solid lines are the $\langle dU/d\lambda \rangle_\lambda$ averages from each of the 4 trials. The shaded region is the standard deviation of $\langle dU/d\lambda \rangle_\lambda$ calculated from the aggregate sampling, and $\langle \sigma \rangle$ is the mean value of the standard deviation. A free energy is calculated for each trial by integrating the corresponding $\langle dU/d\lambda \rangle_\lambda$ profile with trapezoidal-rule integration. $\sigma_{\Delta G}$ is the standard deviation of the 4 free energy estimates.

Table 2. Ring-Flipping Torsion Angle Distributions from Alchemical Free Energy Simulations[a]

Ligand	Simulation	no RE		MCS/E		ACES	
		P_{syn}/P_{anti}	Err	P_{syn}/P_{anti}	Err	P_{syn}/P_{anti}	Err
18	**18 → 19**	0.89/0.11	0.52	0.49/0.51	0.11	0.48/0.52	0.10
	18 → 20	0.69/0.32	0.32	0.52/0.48	0.15	0.53/0.47	0.15
	18 → 21	0.02/0.98	0.36	0.33/0.67	0.04	0.47/0.53	0.09
19	**18 → 19**	0.15/0.85	0.16	0.10/0.90	0.21	0.19/0.81	0.12
	19 → 20	0.71/0.29	0.40	0.10/0.90	0.21	0.39/0.61	0.08
	19 → 21	0.11/0.90	0.20	0.33/0.67	0.02	0.21/0.79	0.10
20	**18 → 20**	1.00/0.00	0.08	0.53/0.47	0.39	0.82/0.18	0.11
	19 → 20	0.11/0.89	0.81	0.89/0.11	0.03	0.88/0.12	0.04
	20 → 21	1.00/0.00	0.07	0.94/0.06	0.02	0.93/0.07	0.01
21	**18 → 21**	0.00/1.00	0.32	0.39/0.61	0.069	0.13/0.87	0.19
	19 → 21	0.92/0.08	0.60	0.67/0.33	0.35	0.25/0.75	0.07
	20 → 21	0.28/0.72	0.04	0.21/0.79	0.11	0.22/0.78	0.10
maE			0.32		0.14		0.10
rmsE			0.39		0.19		0.11

[a] P_{syn} is the probability of observing the ring torsion angle ψ in the range $[-90, 90]$. P_{anti} is the probability of finding it in the range $[90, 270]$. The probabilities are averages over 4 independent trials. The absolute error (Err) is with respect to the ACES self-transformation reference values listed in Table 1.

variation in the free energy estimates. To emphasize this point, Table 2 compares the population of *syn/anti* conformational states observed within the AFE simulations. Specifically, the

table lists the probability ratios of *syn/anti* for each ligand, and the error is relative to the reference ratios shown in Table 1 (the average distribution of the ACES self-transformation end-

Table 3. Relative Binding Free Energy Values ($\Delta\Delta G_b$ in kcal/mol) Calculated from Alchemical Free Energy Simulations[a]

Simulation	no RE		MCS/E		ACES		Expt.
	$\Delta\Delta G_b$	(σ_{err})	$\Delta\Delta G_b$	(σ_{err})	$\Delta\Delta G_b$	(σ_{err})	
18 → 19	−1.73	(0.14)	−1.74	(0.05)	−1.84	(0.04)	−3.11
18 → 20	−0.46	(0.14)	−0.64	(0.07)	−0.76	(0.041)	−0.45
18 → 21	−1.76	(0.12)	−1.62	(0.06)	−1.87	(0.04)	−3.42
19 → 20	1.27	(0.15)	1.11	(0.07)	1.08	(0.04)	2.67
19 → 21	−0.030	(0.13)	0.12	(0.06)	−0.03	(0.03)	−0.31
20 → 21	−1.30	(0.13)	−0.99	(0.078)	−1.11	(0.04)	−2.97
maE	1.068		1.22		1.14		
rmsE	1.26		1.40		1.30		

[a]The $\Delta\Delta G_b$ and σ_{err} values (kcal/mol) are the average and standard error of free energy estimates made from 4 independent sets of simulations. The free energy was calculated by solving the multistate Bennett acceptance ratio (MBAR) equations[91] with cycle closure constraints.[79] The experimental free energies (Expt.) are estimates based on the reported IC_{50} values.[66] "maE" and "rmsE" are the mean absolute error and root-mean-square errors relative to experiment, respectively.
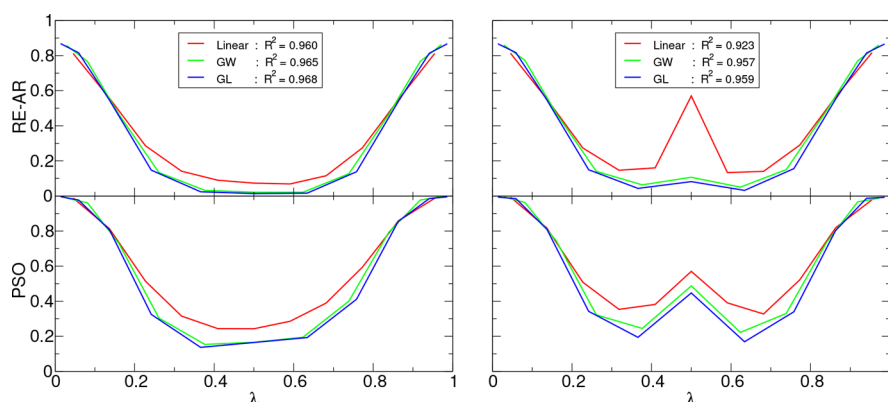

Figure 5. Correlation between phase-space overlap (PSO, bottom) and HREMD acceptance ratio (RE-AR, top) from RBFE simulations of **18 → 21** (left) and **19 → 21** (right) in the protein−ligand environment. The schedules are linear, Golub-Welsch (GW), and the Gauss-Lobatto (GL) quadrature points. The legend lists the linear correlation coefficient (R^2) between PSO and RE-AR for each schedule.

states). The ACES method produces the smallest mean absolute error (maE) and root-mean-square error (rmsE) values (0.10 and 0.11, respectively). In comparison, the maE and rmsE values of "MCS/E" (0.14 and 0.19, respectively) and "no RE" (0.32 and 0.39, respectively) are 1.5-to-3 times larger. The "no RE" simulations exhibit the largest errors in the conformational populations because they do not take advantage of the enhanced sampling offered by HREMD. The MCS/E method, which makes use of HREMD, performs significantly better. It has a mean absolute error of 14%; however, the error in the populations can be as large as 39% (ligand **20** in the **18 → 20** alchemical transformation). The ACES approach performs the best; it has the lowest mean absolute error of 10% and a maximum error of 19% (ligand **21** in the **18 → 21** alchemical transformation).

Table 3 lists the RBFE values ($\Delta\Delta G_b$) and standard errors (σ_{err}) from four independent trials. The "no RE" results have considerably larger standard errors (0.12−0.16 kcal/mol) whereas the maximum standard errors from "MCS/E" and ACES are 0.08 and 0.04 kcal/mol, respectively. The average errors with respect to experiment are generally similar between the methods (maE values 1.1−1.2 kcal/mol). The magnitude of the experimental RBFE values of **18 → 19**, **18 → 21**, and **20 → 21** are approximately 3 kcal/mol, whereas the magnitude of the calculated values are less than 2 kcal/mol. This is likely due to errors in the force field itself for this system. The maE with respect to experiment produced by ACES (1.14 kcal/mol) is slightly less than for "MCS/E" (1.22 kcal/mol); however, the

maE values are within the standard error estimates and not statistically distinguishable.

When taken as a whole, the results presented here demonstrate the advantages of ACES through its use of an expanded softcore region and HREMD to connect the enhanced sampling states.

3.3. Improved Sampling Efficiency from Optimized λ-Scheduling. As illustrated in the previous sections, the ACES approach critically relies on the HREMD framework to facilitate transfer of diverse structures generated in the noninteracting dummy state to the real state with the correct Boltzmann probability. Efficient enhanced sampling is achieved by high-throughput end-to-end conduction of conformational states. The most direct measure of the throughput is the average end-to-end transit time, or so-called "single-pass" time;[68] i.e., the average number of MD steps (or sometimes measured in exchange attempts made at constant time intervals) for a replica to pass from one end state ($\lambda = 0$ or 1) to the other ($\lambda = 1$ or 0). The shorter the average single-pass time, the more single passes are made and the more complete the HREMD/ACES sampling. Replica exchange can be hindered by poor acceptance ratios between λ-intervals that are typically related to having poor phase space overlap[69−72] between adjacent windows. Having even one interval with very low exchange probability (acceptance ratio) can produce a bottleneck that prevents enhanced sampling. Given that the phase space overlaps and related $\langle\partial U/\partial\lambda\rangle_\lambda$ profiles can vary between transformations within a thermodynamic graph, it is difficult to predict *a priori* where
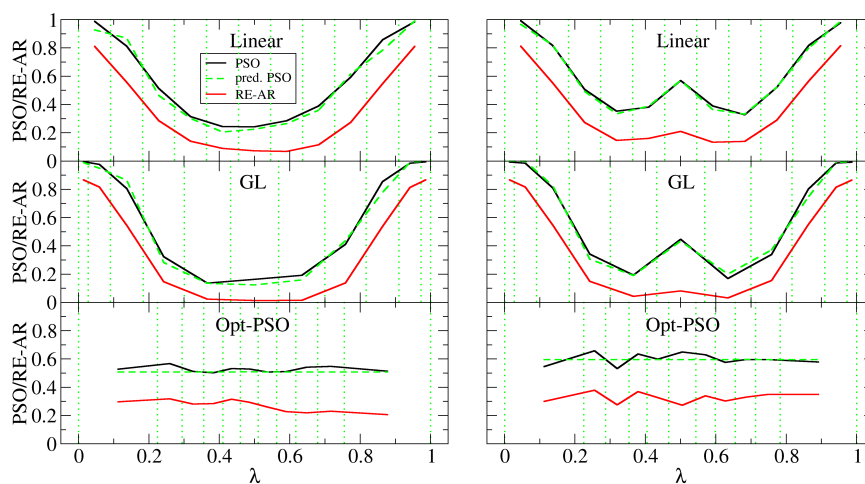
Figure 6. Correlation between the predicted and observed phase-space overlap (PSO) and HREMD acceptance ratio (RE-AR) from the **18 → 21** (left) and **19 → 21** (right) RBFE simulations in the protein−ligand environment. The schedules are linear (top), GL (middle) and Opt-PSO (bottom). Each schedule consists of 12 λ values.

such bottlenecks may occur and how to avoid them in a manner amenable to automation. Phase space overlap and replica exchange acceptance ratio are closely related. Both are sensitive to the alchemical transformation pathway and the spacing between adjacent λ-states.

In this subsection, we present a new method to determine λ-spacing that optimizes the phase space overlap between adjacent λ-states. The method improves the efficiency of the replica-exchange in production simulations. We first set out to illustrate the strong correlation between phase space overlap (PSO) and Hamiltonian replica-exchange acceptance ratio (RE-AR). We illustrate that several commonly used λ-spacing schedules can give considerably different PSO and RE-AR profiles, as well as different average number of end-to-end single-passes and total round trips. Finally, we illustrate that the new method is able to predict the PSO. The predicted PSO is used to determine a schedule of λ-states that equalizes the PSO between intervals. This establishes a new Opt-PSO method for the automated selection of λ-windows based on short burn-in simulations. The burn-in simulations typically increases the direct computational cost by less than 5%.

3.3.1. Correlation between Phase Space Overlap and Replica Exchange Acceptance Ratio. Figure 5 illustrates the correlation between PSO and RE-AR. For this demonstration, we performed **18 → 21** and **19 → 21** AFE simulations in the protein environment with 12 λ-states and 3 λ-schedules. The 3 schedules are "linear" (equally spaced λ-states), "GW" (Golub-Welsch quadrature[92]), and "GL" (Gauss-Lobatto quadrature[93]). The GW schedule does not place values at the end-points λ = 0,1. This choice of λ-spacing has been used for thermodynamic integration,[94,95] especially for alchemical transformation pathways that exhibit numerical instabilities near the end-points. The GW schedule should not be used with free energy perturbation methods that formally require the end-points to be included. In contrast, the GL schedule does include end-point simulations. The simulations were performed for 6 ns in the *NPT* ensemble at 300 K and 1 atm using a 1 fs time step. The PSO and RE-AR values were obtained by analyzing the last 5 ns of the simulations. It is clear from Figure 5 that the PSO and RE-AR are highly correlated for all the λ-schedules in both transformations. The linear correlation coefficients are all greater than 0.9. This correlation provides motivation that the design of

a method that optimizes the phase space overlap to further enhance AFE simulations using ACES.

3.3.2. The Opt-PSO Method. We develop a new method to determine a λ-schedule that optimizes the PSO between adjacent λ-states. The method uses a short "burn-in" ACES simulation with a uniform λ-spacing to quickly accumulate statistics about the nonlocal PSO. In the present work, the burn-in simulations were performed for 600 ps with 21 uniformly spaced λ-windows, and the nonlocal PSO was calculated from the last 500 ps each simulation. The statistics are used to create a smooth 2D map of the predicted PSO between arbitrary placed λ-states. Given the 2D map and the number desired λ-states, a schedule is optimized, as described in the Methods section. The optimized schedule is then used to perform production-length ACES simulations. To make comparison with the results in Figure 5, we optimized schedules consisting of 12 λ-states, and these schedules were simulated with ACES for 6 ns. The last 5 ns of each simulation was used to calculate the observed PSO and RE-AR.

Figure 6 illustrates the PSO and RE-AR for the **18 → 21** (left) and **19 → 21** (right) RBFE simulations in the protein environment using several λ-schedules. Note that the PSO and RE-AR are functions of λ intervals; the λ axis corresponds to the average of the two λ-state values which make up the interval. In other words, although the λ-states span the interval [0, 1] and contain the end-points of 0 and 1, the lines in Figure 6 do not extend to 0 and 1 because the interval-averaged values are used for the λ axis. The simulated λ values are indicated by vertical dotted lines. The green dashed lines in each pane are the predicted PSO of the schedule estimated from nonlocal PSO function parametrized from the 21-window burn-in simulation. The black lines are the observed PSO from the simulations performed with the schedule, and the red lines are the observed RE-AR. It is clear that the PSO values predicted from the burn-in simulations are almost identical to the observed PSO values derived from the production simulation. As illustrated in the previous section, the observed RE-AR values are strongly correlated with the observed PSO.

The new Opt-PSO method determines a λ-schedule by minimizing the variance in the PSO between adjacent states. The predicted PSO of the optimized schedule is shown as the green dashed line in the bottom panels of Figure 6. The observed

Table 4. Ring-Flipping Torsion Angle Distributions from Alchemical Free Energy Simulations with Different λ-Scheduling[a]

		Linear		GL		Opt-PSO	
Ligand	Simulation	P_{syn}/P_{anti}	Err	P_{syn}/P_{anti}	Err	P_{syn}/P_{anti}	Err
18	**18 → 21**	0.54/0.46	0.16	0.52/0.48	0.14	0.46/0.54	0.08
19	**19 → 21**	0.22/0.78	0.09	0.13/0.87	0.18	0.24/0.76	0.07
21	**18 → 21**	0.067/0.93	0.25	0.10/0.90	0.22	0.08/0.92	0.24
	19 → 21	0.23/0.77	0.09	0.13/0.87	0.19	0.19/0.81	0.13
maE			0.15		0.18		0.13
rmsE			0.32		0.37		0.29

[a] P_{syn} is the probability of observing the ring torsion angle ψ in the range $[-90, 90]$. P_{anti} is the probability of finding it in the range $[90, 270]$. The probabilities are averages over 4 independent ACES trials. The absolute error (Err) is with respect to the ACES self-transformation reference values listed in Table 1. Results from different 12-point λ schedules are compared: linear, Gauss-Lobatto quadrature (GL) and optimized phase space overlap (Opt-PSO).

Table 5. Comparison of HREMD Statistics for ACES RBFE Simulations Using Opt-PSO, Linear, and Gaussian Quadrature 12-Point Schedules[a]

		RE-AR			Single Passes		Round Trips		ΔG	
Simulation	λ-spacing	Avg.	(σ)	Min	Avg.	(σ)	Avg.	(σ)	Avg.	(σ_{err})
18 → 21 Complex	Linear	0.34	0.28	0.07	252.67	29.17	120.67	14.82	−3.25	0.11
	GL	0.44	0.35	0.01	125.67	4.03	57.33	2.36	−2.93	0.14
	Opt-PSO	0.27	0.04	0.20	383.00	39.82	187.00	19.61	−3.12	0.19
	Opt-KL	0.22	0.01	0.21	347.67	33.56	169.00	16.31	−3.03	0.05
	Opt-AR	0.26	0.01	0.24	336.67	17.31	163.67	9.03	−3.20	0.14
18 → 21 Aqueous	Linear	0.42	0.31	0.12	1437.00	31.28	713.00	15.64	−0.87	0.03
	GL	0.52	0.40	0.03	732.67	32.89	360.00	16.31	−0.84	0.04
	Opt-PSO	0.35	0.07	0.24	2165.33	15.06	1078.33	7.59	−0.85	0.03
	Opt-KL	0.34	0.04	0.29	2280.00	52.24	1134.33	26.03	−0.87	0.03
	Opt-AR	0.35	0.01	0.32	2293.00	61.65	1140.67	30.62	−0.89	0.02
19 → 21 Complex	Linear	0.37	0.25	0.13	729.33	29.32	359.33	14.82	−7.07	0.10
	GL	0.45	0.34	0.03	441.67	30.47	215.67	15.17	−7.16	0.05
	Opt-PSO	0.33	0.03	0.27	1202.67	15.80	595.67	8.01	−7.15	0.08
	Opt-KL	0.34	0.01	0.33	1252.67	66.68	621.00	33.44	−7.17	0.06
	Opt-AR	0.33	0.01	0.31	1194.00	47.59	591.33	24.28	−7.16	0.09
19 → 21 Aqueous	Linear	0.43	0.29	0.15	1967.00	11.86	978.00	6.16	−7.16	0.03
	GL	0.52	0.39	0.04	1122.33	2.05	555.00	0.82	−7.19	0.03
	Opt-PSO	0.38	0.06	0.28	2708.33	16.74	1348.33	8.18	−7.12	0.02
	Opt-KL	0.40	0.01	0.39	2832.67	10.96	1411.00	4.97	−7.22	0.03
	Opt-AR	0.38	0.01	0.35	2878.33	26.39	1433.33	13.42	−7.15	0.03

[a] Each transformation was simulated 4 times, and the RE-AR, single pass, and round trip values were calculated for each trial. The reported values are the average (Avg.), standard deviation (σ), and minimum value (Min). The free energy (kcal/mol) of each transformation, ΔG was calculated by solving the MBAR equations.[91] The reported free energies are the average (Avg.) and standard error (σ_{err}) from the 4 estimates.

PSO from the production simulation using the Opt-PSO schedule is shown as the solid black line and it is nearly uniform. Similarly, the RE-AR (solid red line) is also close to uniform with respect to the other schedules. These demonstrations provide important validation of the predictive capability of the Opt-PSO method.

Table 5 lists the replica exchange acceptance ratio (average and minimum values), and the number of single passes and total round trips[96,97] for the **18 → 21** and **19 → 21** transformations in the protein environment using 12 λ points with several λ-schedules. The average value of the RE-AR is highest for GL and lowest for Opt-PSO; however, merely looking at the average value is misleading because the linear and GL schedules produce very large RE-AR values near the end-states and very low values near $\lambda = 0.5$. The presence of low RE-AR values causes "bottlenecks" that inhibits enhanced sampling. If one instead compares the minimum RE-AR values, Opt-PSO (0.20−0.28) exhibits larger values than GL (0.01−0.04) and linear (0.07−0.15) schedules. In other words, the GL and linear λ-schedules

exhibit replica exchange bottlenecks in comparison to Opt-PSO. This translates into the Opt-PSO producing a larger number of single passes and round trips. For the examples in Table 5, the Opt-PSO λ-schedule produces roughly 50% more singles passes and round trips than the linear schedule and roughly 200% more than the GL schedule.

Figure 7 illustrates the ring-flipping torsion angle distributions for simulations with (top) and without (bottom) HREMD/ACES using linear, GL and Opt-PSO λ-schedules for the **18 → 21** transformation. A complete set of analogous figures for ligands **18**, **19** and **21** from **18 → 21** and **19 → 21** transformations are provided in the Supporting Information. The real state for ligand **18** corresponds to $\lambda = 0$, whereas the enhanced sampling dummy state corresponds to $\lambda = 1$. The ACES simulations illustrate that the torsion distributions evolve fairly smoothly from the enhanced sampled state to the real state with similar final real-state distributions. Comparison with the corresponding simulations without HREMD illustrate that the torsion distributions between λ states are disconnected and can
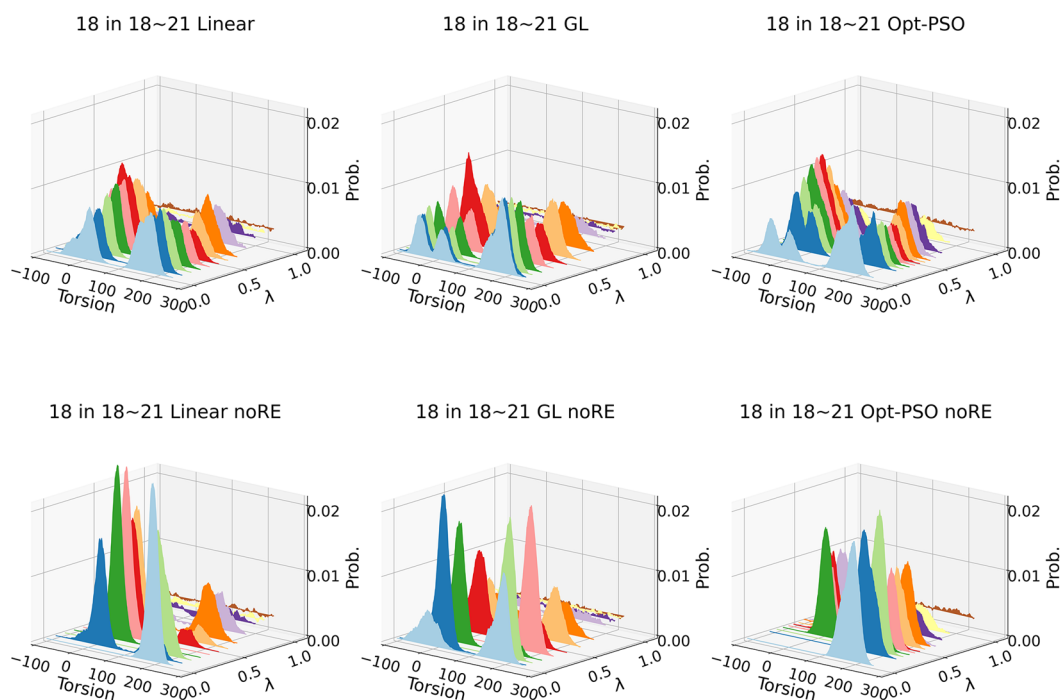
Figure 7. Torsion distributions for all 12 λ windows using linear (left), GL (middle) and Opt-PSO (right) λ-scheduling from HREMD/ACES (top) and no-HREMD (noRE, bottom) simulations for ligand **18** in the **18** → **21** protein–ligand environment.

Table 6. HREMD Statistics from ACES RBFE Simulations Using Opt-PSO Schedules of Various Sizes[a]

Simulation	N	RE-AR			Single Passes		Round Trips		ΔG	
		Avg.	(σ)	Min	Avg.	(σ)	Avg.	(σ)	Avg.	(σ_{err})
18 → **21** Complex	8	0.11	0.04	0.04	195.00	5.66	94.33	2.62	−3.09	0.24
	12	0.27	0.04	0.20	383.00	39.82	187.00	19.61	−3.12	0.19
	16	0.39	0.04	0.33	557.00	37.59	272.33	18.93	−3.04	0.12
	20	0.48	0.03	0.42	642.67	13.57	312.67	6.60	−3.20	0.06
	24	0.54	0.03	0.49	710.33	72.83	345.67	35.80	−3.21	0.09
18 → **21** Aqueous	8	0.15	0.03	0.09	1208.00	24.34	601.00	12.03	−0.94	0.03
	12	0.35	0.07	0.24	2165.33	15.06	1078.33	7.59	−0.85	0.03
	16	0.49	0.04	0.42	3096.67	2.49	1541.67	0.47	−0.87	0.02
	20	0.59	0.03	0.52	3823.33	31.79	1903.33	15.28	−0.87	0.01
	24	0.65	0.03	0.60	4521.00	23.28	2249.67	11.47	−0.89	0.01
19 → **21** Complex	8	0.17	0.06	0.04	603.67	37.61	297.67	19.22	−6.99	0.11
	12	0.33	0.03	0.27	1202.67	15.80	595.67	8.01	−7.15	0.08
	16	0.45	0.02	0.39	1583.33	74.70	784.00	37.50	−7.06	0.10
	20	0.53	0.02	0.48	1876.00	86.30	928.33	43.48	−7.11	0.07
	24	0.58	0.02	0.55	2114.67	60.61	1066.00	1.63	−7.02	0.02
19 → **21** Aqueous	8	0.19	0.08	0.07	1468.67	32.74	730.00	16.39	−7.20	0.04
	12	0.38	0.06	0.28	2708.33	16.74	1348.33	8.18	−7.12	0.02
	16	0.52	0.07	0.43	3733.33	18.21	1859.33	8.96	−7.12	0.03
	20	0.61	0.07	0.54	4607.00	50.94	2294.00	25.46	−7.18	0.02
	24	0.67	0.06	0.61	5327.67	57.28	2652.33	29.01	−7.14	0.01

[a]N is the number λ-states in the schedule. Each transformation was simulated 4 times, and the RE-AR, single pass, and round trip values were calculated for each trial. The reported values are the average (Avg.), standard deviation (σ), and minimum value (Min). The free energy (kcal/mol) of each transformation, ΔG was calculated by solving the MBAR equations.[91] The reported free energies are the average (Avg.) and standard error (σ_{err}) from the 4 estimates.

become trapped. This is exemplified for the real state torsion distributions in both the linear and Opt-PSO schedules without HREMD (Figure 7, bottom row). Table 4 compares the P_{syn}/P_{anti} values from **18** → **21** and **19** → **21** ACES transformations using different 12-point λ schedules. Overall, the Opt-PSO λ

schedule has the closest agreement (lowest maE and rmsE values) with respect to the reference values listed in Table 1.

Table 6 lists replica exchange statistics for **18** → **21** and **19** → **21** transformations using the Opt-PSO method with different number of λ points. The average and minimum value for the RE-AR monotonically increases with the number of λ states, as do
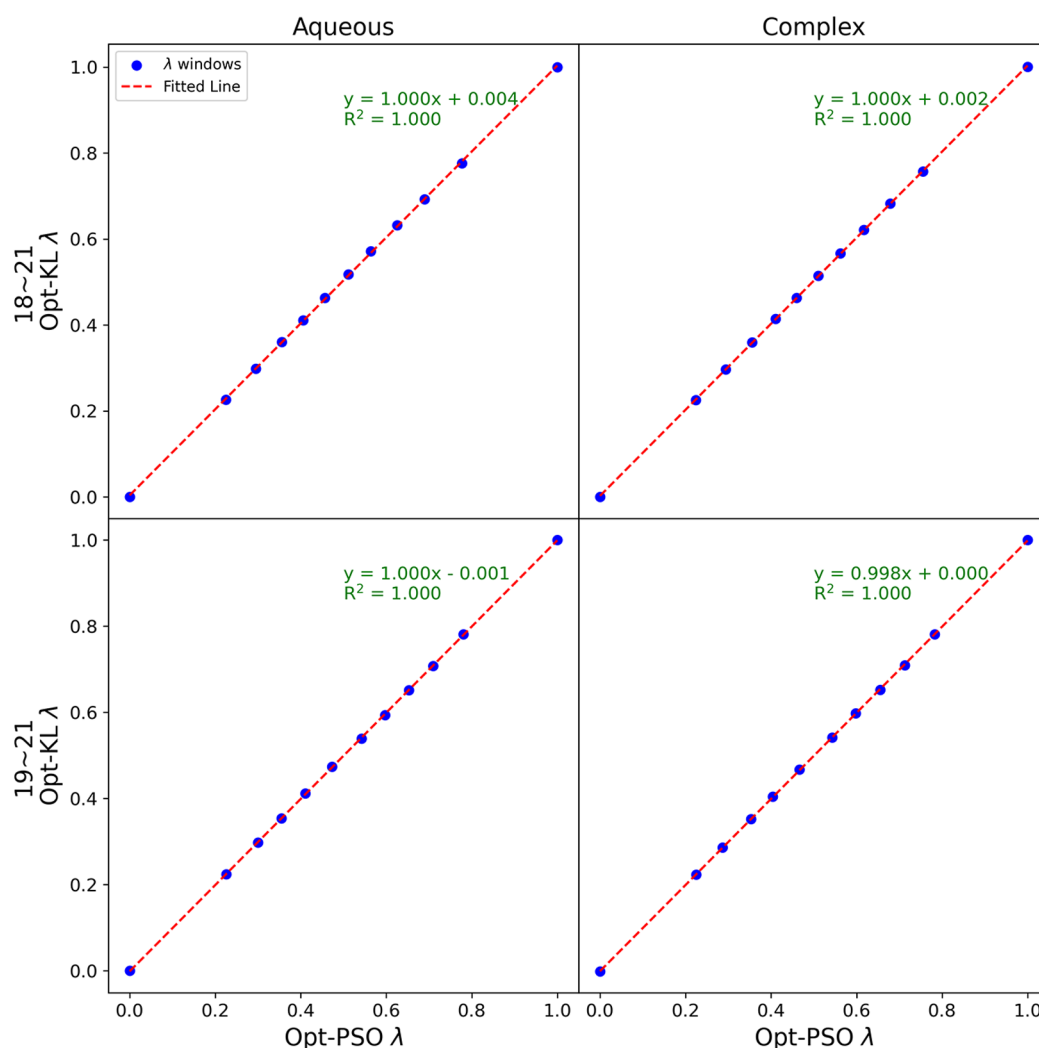
Figure 8. Correlation between the Opt-PSO and Opt-KL from the **18 → 21** (top) and **19 → 21** (bottom) RBFE burn-in simulations in both aqueous and protein−ligand environment. Each schedule consists of 12 λ values.

the number of end-to-end single passes and total round trips. The free energy values are all within 0.3 kcal/mol, and the standard error estimates generally decrease with increasing number of λ points. Taken together, the results presented here demonstrate a new procedure for customizing the λ-schedule that increases the efficiency and robustness of alchemical free energy simulations using ACES.

3.3.3. Alternative Optimized Kullback−Leibler (KL) Divergence and Acceptance Ratio (AR) Methods. In this section we compare alternative methods to the optimized phase space overlap (Opt-PSO) based on 2D maps of quantities that represent the Kullback−Leibler divergence and HREMD acceptance ratio that we designate Opt-KL and Opt-AR, respectively. These variations are described in detail in the Methods section.

A concern regarding the use of the PSO index involves the use of a max() function in eq 5 that could introduce numerical instabilities. As an alternative (suggested in peer review), an index based on the Kullback−Leibler (KL) divergence was explored and the resulting λ schedule designated Opt-KL. For the systems studies here, this index produced a 12-point Opt-KL λ-schedule that was nearly identical to the Opt-PSO λ-schedule as illustrated in Figure 8. Analysis of λ-schedules for different

number of λ points ranging from 8 to 24 shows that only for the 8-point schedule derived from the **18 → 21** burn-in does the R^2 correlation between λ-schedules drop below 0.9.

In order to gain further insight into the nature of the differences between the Opt-PSO and Opt-KL λ schedules, the 2D maps derived from the **18 → 21** and **19 → 21** burn-in simulations are shown in Figure 9. Using the PSO index as an example (left column in Figure 9), the way to interpret the 2D maps are as follows. The value of the 2D map at the point (λ_1, λ_2) is the predicted PSO for the λ-interval. The goal than is to determine a set of N_λ points such that the value of the PSO is uniform for all λ-intervals, forming an isocontour line in the 2D map. These points are illustrated $N_\lambda = 12$ as black dots in Figure 9. In order to achieve this, it is desirable that the index being mapped decays monotonically from the diagonal in both the λ_1 and λ_2 directions such that the solution for the isocontour lines is unique and continuous.

Examination of Figure 9 shows that the PSO (left) and KL (middle) maps are quite similar. However, somewhat disconcerting is that both of these indexes do not monotonically decay from the diagonal. This implies that, for a fixed values of λ_1, there could be multiple values of λ_2 that have the same value of the PSO or KL indexes. This is not a serious issue if the
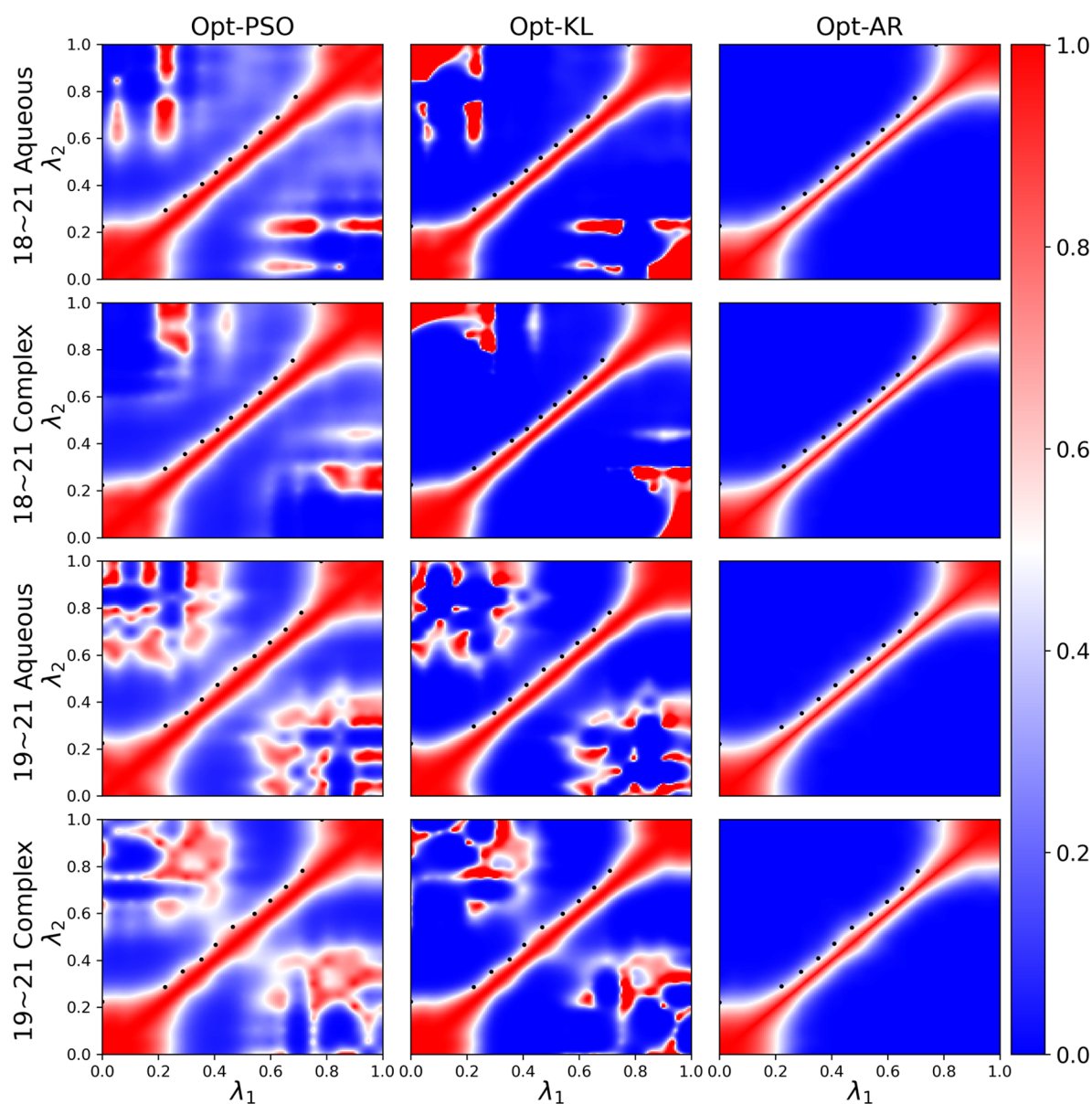
Figure 9. 2D maps of phase space overlap (PSO) index of eq 5, Kullback−Leibler (KL) divergence index of eq 20, and HREMD acceptance ratio (AR) index of eq 22 based on the same burn-in simulations for the $18 \rightarrow 21$ and $19 \rightarrow 21$ transformations in the complex and aqueous phase. Black dots are illustrated for the optimized 12-λ point schedules.

number of λ points is large enough such that the λ intervals become sufficiently small. Nonetheless, determination of what constitutes "sufficiently small" might be difficult to ascertain *a priori* for more general cases. To address this issue, we explored the use of an "acceptance ration" (AR) index closely related to the Metropolis criterion used in HREMD simulations at constant temperature. The 2D maps of this index are shown as the rightmost set of panels in Figure 9 and monotonically decay. The Opt-AR λ-schedules are highly correlated to both the Opt-PSO and Opt-KL λ-schedules as indicated in Table S1 of the Supporting Information (with exceptions seen only in certain instances for the 8-point λ-schedules).

Table 5 compares the HREMD statistics for the 12-point Opt-PSO, Opt-KL and Opt-AR λ-schedules. The results are all fairly similar to all three methods performing considerable better than the linear and GL λ schedules. For the systems considered, the Opt-PSO, Opt-KL and Opt-AR methods appear quite

comparable with none of them having a significant performance advantage. Nonetheless, considering the monotonic decay behavior of the 2D maps using the AR index, the Opt-AR method may have greater stability and advantages if integrated into an automated procedure for determination of optimal λ schedules for alchemical free energy simulations.

4. CONCLUSIONS

The results presented here illustrate the advantages of ACES for conformational sampling of ring flipping in ML300-derived noncovalent inhibitors of SARS-CoV-2 M^{pro}. Unlike traditional MD simulations, ACES is demonstrated to give consistent *syn/anti* distributions regardless of starting conformation. The ACES method is further applied to the calculation of RBFEs, and the effect of replica exchange and the choice of softcore region was investigated. The results are used to gain insight into the factors that enable ACES to improve importance sampling and achieve

high precision free energy estimates. Furthermore, we examined how the efficiency of ACES was affected by the degree of phase space overlap between adjacent states (i.e., between neighboring λ-windows). We developed and tested a new procedure for customizing the λ-schedule from the analysis of short, burn-in ACES simulations. The method was shown to increase replica exchange efficiency in alchemical free energy simulations. It remains to further test the method against a broader range of relative and absolute binding free energy simulations that include transformations of ligands forming a congeneric series, as well as ligands that have different scaffolds. It is through application of the methods to a diverse series of transformations that a set of recommended best practices and automated workflows may emerge.

ASSOCIATED CONTENT

ⓈⒾ Supporting Information

The Supporting Information is available free of charge at https://pubs.acs.org/doi/10.1021/acs.jctc.4c00251.

> Correlation of the Opt-PSO, Opt-KL and Opt-AR based on the **18 → 21** and **19 → 21** burn-in simulations and analyses of the torsion angle distributions as a function of λ for ligands **18**, **19** and **21** from **18 → 21** and **19 → 21** transformations using different λ-scheduling, with and without using replica exchange (PDF)

AUTHOR INFORMATION

Corresponding Author

Darrin M. York − *Laboratory for Biomolecular Simulation Research, Institute for Quantitative Biomedicine and Department of Chemistry and Chemical Biology, Rutgers University, Piscataway, New Jersey 08854, United States;* ⓞ orcid.org/0000-0002-9193-7055; Email: Darrin.York@rutgers.edu

Authors

Shi Zhang − *Laboratory for Biomolecular Simulation Research, Institute for Quantitative Biomedicine and Department of Chemistry and Chemical Biology, Rutgers University, Piscataway, New Jersey 08854, United States;* ⓞ orcid.org/0000-0002-0281-9314

Timothy J. Giese − *Laboratory for Biomolecular Simulation Research, Institute for Quantitative Biomedicine and Department of Chemistry and Chemical Biology, Rutgers University, Piscataway, New Jersey 08854, United States;* ⓞ orcid.org/0000-0002-0653-9168

Tai-Sung Lee − *Laboratory for Biomolecular Simulation Research, Institute for Quantitative Biomedicine and Department of Chemistry and Chemical Biology, Rutgers University, Piscataway, New Jersey 08854, United States;* ⓞ orcid.org/0000-0003-2110-2279

Complete contact information is available at:
https://pubs.acs.org/10.1021/acs.jctc.4c00251

Notes

The authors declare no competing financial interest.

ACKNOWLEDGMENTS

REFERENCES

(1) York, D. M. Modern Alchemical Free Energy Methods for Drug Discovery Explained. *ACS Phys. Chem. Au* **2023**, *3*, 478−491.

(2) Liu, S.; Wu, Y.; Lin, T.; Abel, R.; Redmann, J. P.; Summa, C. M.; Jaber, V. R.; Lim, N. M.; Mobley, D. L. Lead optimization mapper: automating free energy calculations for lead optimization. *J. Comput.-Aided Mol. Des.* **2013**, *27*, 755−770.

(3) Cournia, Z.; Allen, B.; Sherman, W. Relative Binding Free Energy Calculations in Drug Discovery: Recent Advances and Practical Considerations. *J. Chem. Inf. Model.* **2017**, *57*, 2911−2937.

(4) Lee, T.-S.; Allen, B. K.; Giese, T. J.; Guo, Z.; Li, P.; Lin, C.; McGee, T. D.; Pearlman, D. A.; Radak, B. K.; Tao, Y.; et al. Alchemical Binding Free Energy Calculations in AMBER20: Advances and Best Practices for Drug Discovery. *J. Chem. Inf.. Model.* **2020**, *60*, 5595−5623.

(5) Mobley, D. L.; Klimovich, P. V. Perspective: Alchemical free energy calculations for drug discovery. *J. Chem. Phys.* **2012**, *137*, 230901.

(6) Aldeghi, M.; Heifetz, A.; Bodkin, M. J.; Knapp, S.; Biggin, P. C. Predictions of Ligand Selectivity from Absolute Binding Free Energy Calculations. *J. Am. Chem. Soc.* **2017**, *139*, 946−957.

(7) Chodera, J.; Mobley, D.; Shirts, M.; Dixon, R.; Branson, K.; Pande, V. Alchemical free energy methods for drug discovery: progress and challenges. *Curr. Opin. Struct. Biol.* **2011**, *21*, 150−160.

(8) Jorgensen, W. L. Efficient drug lead discovery and optimization. *Acc. Chem. Res.* **2009**, *42*, 724−733.

(9) Azimi, S.; Khuttan, S.; Wu, J. Z.; Pal, R. K.; Gallicchio, E. Relative Binding Free Energy Calculations for Ligands with Diverse Scaffolds with the Alchemical Transfer Method. *J. Chem. Inf. Model.* **2022**, *62*, 309−323.

(10) Papadourakis, M.; Sinenka, H.; Matricon, P.; Hénin, J.; Brannigan, G.; Pérez-Benito, L.; Pande, V.; van Vlijmen, H.; de Graaf, C.; Deflorian, F.; et al. Alchemical Free Energy Calculations on Membrane-Associated Proteins. *J. Chem. Theory Comput.* **2023**, *19*, 7437−7458.

(11) Sliwoski, G.; Kothiwale, S.; Meiler, J.; Lowe, E. W., Jr Computational Methods in Drug Discovery. *Pharmacol. Rev.* **2014**, *66*, 334−95.

(12) Van Drie, J. H. Computer-aided drug design: the next 20 years. *J. Comput.-Aided Mol. Des.* **2007**, *21*, 591−601.

(13) Chen, L.; Wu, Y.; Wu, C.; Silveira, A.; Sherman, W.; Xu, H.; Gallicchio, E. Performance and Analysis of the Alchemical Transfer Method for Binding-Free-Energy Predictions of Diverse Ligands. *J. Chem. Inf. Model.* **2024**, *64*, 250−264.

(14) Fu, H.; Chen, H.; Cai, W.; Shao, X.; Chipot, C. BFEE2: Automated, Streamlined, and Accurate Absolute Binding Free-Energy Calculations. *J. Chem. Inf. Model.* **2021**, *61*, 2116−2123.

(15) Gapsys, V.; Yildirim, A.; Aldeghi, M.; Khalak, Y.; van der Spoel, D.; de Groot, B. L. Accurate absolute free energies for ligand−protein binding based on non-equilibrium approaches. *Commun. Chem.* **2021**, *4*, 61.

(16) Shobana, S.; Roux, B.; Andersen, O. S. Free Energy Simulations: Thermodynamic Reversibility and Variability. *J. Phys. Chem. B* **2000**, *104*, 5179−5190.

(17) Boresch, S. The Role of Bonded Energy Terms in Free Energy Simulations - Insights from Analytical Results. *Mol. Simul.* **2002**, *28*, 13−37.

Journal of Chemical Theory and Computation
pubs.acs.org/JCTC
Article

(18) Fleck, M.; Wieder, M.; Boresch, S. Dummy Atoms in Alchemical Free Energy Calculations. *J. Chem. Theory Comput.* **2021**, *17*, 4403−4419.

(19) Beutler, T. C.; Mark, A. E.; van Schaik, R. C.; Gerber, P. R.; van Gunsteren, W. F. Avoiding singularities and numerical instabilities in free energy calculations based on molecular simulations. *Chem. Phys. Lett.* **1994**, *222*, 529−539.

(20) Steinbrecher, T.; Joung, I.; Case, D. A. Soft-Core Potentials in Thermodynamic Integration: Comparing One- and Two-Step Transformations. *J. Comput. Chem.* **2011**, *32*, 3253−3263.

(21) Hornak, V.; Simmerling, C. Development of softcore potential functions for overcoming steric barriers in molecular dynamics simulations. *J. Mol. Graphics Model.* **2004**, *22*, 405−413.

(22) Giese, T. J.; York, D. M. A GPU-Accelerated Parameter Interpolation Thermodynamic Integration Free Energy Method. *J. Chem. Theory Comput.* **2018**, *14*, 1564−1582.

(23) Gapsys, V.; Seeliger, D.; de Groot, B. L. New Soft-Core Potential Function for Molecular Dynamics Based Alchemical Free Energy Calculations. *J. Chem. Theory Comput.* **2012**, *8*, 2373−2382.

(24) Buelens, F. P.; Grubmüller, H. Linear-scaling soft-core scheme for alchemical free energy calculations. *J. Comput. Chem.* **2012**, *33*, 25−33.

(25) Pal, R. K.; Gallicchio, E. Perturbation potentials to overcome order/disorder transitions in alchemical binding free energy calculations. *J. Chem. Phys.* **2019**, *151*, 124116.

(26) Mezei, M. Polynomial path for the calculation of liquid state free energies from computer simulations tested on liquid water. *J. Comput. Chem.* **1992**, *13*, 651−656.

(27) Resat, H.; Mezei, M. Studies on free energy calculations. I. Thermodynamic integration using a polynomial path. *J. Chem. Phys.* **1993**, *99*, 6052−6061.

(28) Simonson, T. Free energy of particle insertion. *Mol. Phys.* **1993**, *80*, 441−447.

(29) Steinbrecher, T.; Mobley, D. L.; Case, D. A. Nonlinear scaling schemes for Lennard-Jones interactions in free energy calculations. *J. Chem. Phys.* **2007**, *127*, 214108.

(30) Jiang, W.; Chipot, C.; Roux, B. Computing Relative Binding Affinity of Ligands to Receptor: An Effective Hybrid Single-Dual-Topology Free-Energy Perturbation Approach in NAMD. *J. Chem. Inf. Model.* **2019**, *59*, 3794−3802.

(31) Min, D.; Li, H.; Li, G.; Bitetti-Putzer, R.; Yang, W. Synergistic approach to improve "alchemical" free energy calculation in rugged energy surface. *J. Chem. Phys.* **2007**, *126*, 144109.

(32) Cuendet, M. A.; Tuckerman, M. E. Alchemical Free Energy Differences in Flexible Molecules from Thermodynamic Integration or Free Energy Perturbation Combined with Driven Adiabatic Dynamics. *J. Chem. Theory Comput.* **2012**, *8*, 3504−3512.

(33) Gallicchio, E.; Levy, R. M. Advances in all atom sampling methods for modeling protein-ligand binding affinities. *Curr. Opin. Struct. Biol.* **2011**, *21*, 161−166.

(34) Bernardi, R. C.; Melo, M. C. R.; Schulten, K. Enhanced sampling techniques in molecular dynamics simulations of biological systems. *Biochim. Biophys. Acta* **2015**, *1850*, 872−877.

(35) Mitsutake, A.; Mori, Y.; Okamoto, Y. Enhanced sampling algorithms. *Methods Mol. Biol.* **2013**, *924*, 153−195.

(36) Yang, Y. I.; Shao, Q.; Zhang, J.; Yang, L.; Gao, Y. Q. Enhanced sampling in molecular dynamics. *J. Chem. Phys.* **2019**, *151*, 070902.

(37) Wan, S.; Tresadern, G.; Pérez-Benito, L.; van Vlijmen, H.; Coveney, P. V. Accuracy and Precision of Alchemical Relative Free Energy Predictions with and without Replica-Exchange. *Adv. Theory Simul.* **2020**, *3*, 1900195.

(38) Invernizzi, M.; Piaggi, P. M.; Parrinello, M. Unified Approach to Enhanced Sampling. *Phys. Rev. X* **2020**, *10*, 041034.

(39) Hénin, J.; Lelièvre, T.; Shirts, M. R.; Valsson, O.; Delemotte, L. Enhanced Sampling Methods for Molecular Dynamics Simulations [Article v1.0]. *LiveCoMS* **2022**, *4*, 1583.

(40) Khuttan, S.; Gallicchio, E. What to Make of Zero: Resolving the Statistical Noise from Conformational Reorganization in Alchemical Binding Free Energy Estimates with Metadynamics Sampling. *J. Chem. Theory Comput.* **2024**, *20*, 1489−1501.

(41) Abel, R.; Wang, L.; Harder, E. D.; Berne, B. J.; Friesner, R. A. Advancing Drug Discovery through Enhanced Free Energy Calculations. *Acc. Chem. Res.* **2017**, *50*, 1625−1632.

(42) Cournia, Z.; Allen, B. K.; Beuming, T.; Pearlman, D. A.; Radak, B. K.; Sherman, W. Rigorous Free Energy Simulations in Virtual Screening. *J. Chem. Inf. Model.* **2020**, *60*, 4153−4169.

(43) Song, L. F.; Merz, K. M. Evolution of Alchemical Free Energy Methods in Drug Discovery. *J. Chem. Inf. Model.* **2020**, *60*, 5308−5318.

(44) Mey, A. S. J. S.; Allen, B. K.; Macdonald, H. E. B.; Chodera, J. D.; Hahn, D. F.; Kuhn, M.; Michel, J.; Mobley, D. L.; Naden, L. N.; Prasad, S.; et al. Best Practices for Alchemical Free Energy Calculations [Article v1.0]. *LiveCoMS* **2020**, *2*, 18378−18429.

(45) Cournia, Z.; Chipot, C.; Roux, B.; York, D. M.; Sherman, W. In *Free Energy Methods in Drug Discovery—Introduction*; Armacost, K. A., Thompson, D. C., Eds.; ACS Symposium Series; American Chemical Society, 2021; Vol. *1397*, pp 1−38.

(46) Lee, T.-S.; Tsai, H.-C.; Ganguly, A.; York, D. M. ACES: Optimized Alchemically Enhanced Sampling. *J. Chem. Theory Comput.* **2023**, *19*, 472−487.

(47) de Ruiter, A.; Oostenbrink, C. Free energy calculations of protein-ligand interactions. *Curr. Opin. Chem. Biol.* **2011**, *15*, 547−552.

(48) Mentes, A.; Deng, N.-J.; Vijayan, R. S. K.; Xia, J.; Gallicchio, E.; Levy, R. M. Binding Energy Distribution Analysis Method: Hamiltonian Replica Exchange with Torsional Flattening for Binding Mode Prediction and Binding Free Energy Estimation. *J. Chem. Theory Comput.* **2016**, *12*, 2459−2470.

(49) Hahn, D. F.; König, G.; Hünenberger, P. H. Overcoming Orthogonal Barriers in Alchemical Free Energy Calculations: On the Relative Merits of λ-Variations, λ-Extrapolations, and Biasing. *J. Chem. Theory Comput.* **2020**, *16*, 1630−1645.

(50) Liu, P.; Kim, B.; Friesner, R. A.; Berne, B. J. Replica exchange with solute tempering: A method for sampling biological systems in explicit water. *Proc. Natl. Acad. Sci. U.S.A.* **2005**, *102*, 13749−13754.

(51) Wang, L.; Friesner, R. A.; Berne, B. Replica Exchange with Solute Scaling: A More Efficient Version of Replica Exchange with Solute Tempering (REST2). *J. Phys. Chem. B* **2011**, *115*, 9431−9438.

(52) Li, H.; Fajer, M.; Yang, W. Simulated scaling method for localized enhanced sampling and simultaneous "alchemical" free energy simulations: a general method for molecular mechanical, quantum mechanical, and quantum mechanical/molecular mechanical simulations. *J. Chem. Phys.* **2007**, *126*, 24106.

(53) Zheng, L.; Yang, W. Practically Efficient and Robust Free Energy Calculations: Double- Integration Orthogonal Space Tempering. *J. Chem. Theory Comput.* **2012**, *8*, 810−823.

(54) Kaus, J. W.; McCammon, J. A. Enhanced ligand sampling for relative protein-ligand binding free energy calculations. *J. Phys. Chem. B* **2015**, *119*, 6190−6197.

(55) Sidler, D.; Cristòfol-Clough, M.; Riniker, S. Efficient Round-Trip Time Optimization for Replica-Exchange Enveloping Distribution Sampling (RE-EDS). *J. Chem. Theory Comput.* **2017**, *13*, 3020−3030.

(56) König, G.; Glaser, N.; Schroeder, B.; Kubincová, A.; Hünenberger, P. H.; Riniker, S. An Alternative to Conventional λ-Intermediate States in Alchemical Free Energy Calculations: λ-Enveloping Distribution Sampling. *J. Chem. Inf. Model.* **2020**, *60*, 5407−5423.

(57) König, G.; Ries, B.; Hünenberger, P. H.; Riniker, S. Efficient Alchemical Intermediate States in Free Energy Calculations Using λ-Enveloping Distribution Sampling. *J. Chem. Theory Comput.* **2021**, *17*, 5805−5815.

(58) Baumann, H. M.; Dybeck, E.; McClendon, C. L.; Pickard, F. C., 4th; Gapsys, V.; Pérez-Benito, L.; Hahn, D. F.; Tresadern, G.; Mathiowetz, A. M.; Mobley, D. L. Broadening the Scope of Binding Free Energy Calculations Using a Separated Topologies Approach. *J. Chem. Theory Comput.* **2023**, *19*, 5058−5076.

(59) Rieder, S. R.; Ries, B.; Schaller, K.; Champion, C.; Barros, E. P.; Hünenberger, P. H.; Riniker, S. Replica-Exchange Enveloping Distribution Sampling Using Generalized AMBER Force-Field Top-

ologies: Application to Relative Hydration Free-Energy Calculations for Large Sets of Molecules. *J. Chem. Inf. Model.* **2022**, *62*, 3043−3056.

(60) Champion, C.; Gall, R.; Ries, B.; Rieder, S. R.; Barros, E. P.; Riniker, S. Accelerating Alchemical Free Energy Prediction Using a Multistate Method: Application to Multiple Kinases. *J. Chem. Inf. Model.* **2023**, *63*, 7133−7147.

(61) Azimi, S.; Wu, J. Z.; Khuttan, S.; Kurtzman, T.; Deng, N.; Gallicchio, E. Application of the alchemical transfer and potential of mean force methods to the SAMPL8 host-guest blinded challenge. *J. Comput.-Aided Mol. Des.* **2022**, *36*, 63−76.

(62) Sabanés Zariquiey, F.; Pérez, A.; Majewski, M.; Gallicchio, E.; De Fabritiis, G. Validation of the Alchemical Transfer Method for the Estimation of Relative Binding Affinities of Molecular Series. *J. Chem. Inf. Model.* **2023**, *63*, 2438−2444.

(63) Tsai, H.-C.; Lee, T.-S.; Ganguly, A.; Giese, T. J.; Ebert, M. C.; Labute, P.; Merz, K. M., Jr; York, D. M. AMBER Free Energy Tools: A New Framework for the Design of Optimized Alchemical Transformation Pathways. *J. Chem. Theory Comput.* **2023**, *19*, 640−658.

(64) Turlington, M.; Chun, A.; Tomar, S.; Eggler, A.; Grum-Tokars, V.; Jacobs, J.; Daniels, J. S.; Dawson, E.; Saldanha, A.; Chase, P.; et al. Discovery of N-(benzo[1,2,3]triazol-1-yl)-N-(benzyl)acetamido)-phenyl) carboxamides as severe acute respiratory syndrome coronavirus (SARS-CoV) 3CLpro inhibitors: Identification of ML300 and noncovalent nanomolar inhibitors with an induced-fit binding. *Bioorg. Med. Chem. Lett.* **2013**, *23*, 6172−6177.

(65) Zhang, L.; Lin, D.; Sun, X.; Curth, U.; Drosten, C.; Sauerhering, L.; Becker, S.; Rox, K.; Hilgenfeld, R. Crystal structure of SARS-CoV-2 main protease provides a basis for design of improved α-ketoamide inhibitors. *Science* **2020**, *368*, 409−412.

(66) Han, S. H.; Goins, C. M.; Arya, T.; Shin, W.-J.; Maw, J.; Hooper, A.; Sonawane, D. P.; Porter, M. R.; Bannister, B. E.; Crouch, R. D.; et al. Structure-Based Optimization of ML300-Derived, Noncovalent Inhibitors Targeting the Severe Acute Respiratory Syndrome Coronavirus 3CL Protease (SARS-CoV-2 3CL^{pro}). *J. Med. Chem.* **2022**, *65*, 2880−2904.

(67) Kamiya, M.; Sugita, Y. Flexible selection of the solute region in replica exchange with solute tempering: Application to protein-folding simulations. *J. Chem. Phys.* **2018**, *149*, 72304.

(68) Abraham, M. J.; Gready, J. E. Ensuring Mixing Efficiency of Replica-Exchange Molecular Dynamics Simulations. *J. Chem. Theory Comput.* **2008**, *4*, 1119−1128.

(69) Kofke, D. A.; Cummings, P. T. Quantitaive comparison and optimization of methods for evaluating the chemical potential by molecular simulation. *Mol. Phys.* **1997**, *92*, 973−996.

(70) Wu, D.; Kofke, D. A. Phase-space overlap measures. II. Design and implementation of staging methods for free-energy calculations. *J. Chem. Phys.* **2005**, *123*, 84109.

(71) Kofke, D. A. On the sampling requirements for exponential-work free-energy calculations. *Mol. Phys.* **2006**, *104*, 3701−3708.

(72) Giese, T. J.; York, D. M. Development of a Robust Indirect Approach for MM → QM Free Energy Calculations That Combines Force-Matched Reference Potential and Bennett's Acceptance Ratio Methods. *J. Chem. Theory Comput.* **2019**, *15*, 5543−5562.

(73) Kullback, S.; Leibler, R. A. On Information and Sufficiency. *Ann. Math. Statist.* **1951**, *22*, 79−86.

(74) Nocedal, J. Updating quasi-Newton matrices with limited storage. *Math. Comput.* **1980**, *35*, 773−782.

(75) Virtanen, P.; Gommers, R.; Oliphant, T. E.; Haberland, M.; Reddy, T.; Cournapeau, D.; Burovski, E.; Peterson, P.; Weckesser, W.; Bright, J.; et al. SciPy 1.0: fundamental algorithms for scientific computing in Python. *Nat. Methods* **2020**, *17*, 261−272.

(76) Lee, T.-S.; Tsai, H.-C.; Ganguly, A.; Giese, T. J.; York, D. M. In *Robust, Efficient and Automated Methods for Accurate Prediction of Protein-Ligand Binding Affinities in AMBER Drug Discovery Boost*; Armacost, K. A., Thompson, D. C., Eds.; ACS Symposium Series; American Chemical Society, 2021; Vol. *1397*, pp 161−204.

(77) Case, D. A.; Aktulga, H. M.; Belfon, K.; Ben-Shalom, I. Y.; Berryman, J.; Brozell, S. R.; Cerutti, D. S.; Cheatham III, T. E.;

Cruzeiro, V. W. D.; Darden, T. A. et al. *AMBER22*; University of California, San Francisco: San Francisco, CA, 2022.

(78) Giese, T. J.; Ekesan, Ş.; York, D. M. Extension of the Variational Free Energy Profile and Multistate Bennett Acceptance Ratio Methods for High-Dimensional Potential of Mean Force Profile Analysis. *J. Phys. Chem. A* **2021**, *125*, 4216−4232.

(79) Giese, T. J.; York, D. M. Variational Method for Networkwide Analysis of Relative Ligand Binding Free Energies with Loop Closure and Experimental Constraints. *J. Chem. Theory Comput.* **2021**, *17*, 1326−1336.

(80) Case, D. A.; Aktulga, H. M.; Belfon, K.; Cerutti, D. S.; Cisneros, G. A.; Cruzeiro, V. W. D.; Forouzesh, N.; Giese, T. J.; Götz, A. W.; Gohlke, H.; et al. AmberTools. *J. Chem. Inf. Model.* **2023**, *63*, 6183−6191.

(81) Ganguly, A.; Tsai, H.-C.; Fernández-Pendás, M.; Lee, T.-S.; Giese, T. J.; York, D. M. AMBER Drug Discovery Boost Tools: Automated Workflow for Production Free-Energy Simulation Setup and Analysis (ProFESSA). *J. Chem. Inf. Model.* **2022**, *62*, 6069−6083.

(82) He, X.; Man, V. H.; Yang, W.; Lee, T.-S.; Wang, J. A fast and high-quality charge model for the next generation general AMBER force field. *J. Chem. Phys.* **2020**, *153*, 114502.

(83) Horn, H. W.; Swope, W. C.; Pitera, J. W.; Madura, J. D.; Dick, T. J.; Hura, G. L.; Head-Gordon, T. Development of an improved four-site water model for biomolecular simulations: TIP4P-Ew. *J. Chem. Phys.* **2004**, *120*, 9665−9678.

(84) Joung, I. S.; Cheatham, T. E., III Determination of alkali and halide monovalent ion parameters for use in explicitly solvated biomolecular simulations. *J. Phys. Chem. B* **2008**, *112*, 9020−9041.

(85) Joung, I. S.; Cheatham, T. E., III Molecular dynamics simulations of the dynamic and energetic properties of alkali and halide ions using water-model-specific ion parameters. *J. Phys. Chem. B* **2009**, *113*, 13279−13290.

(86) Loncharich, R. J.; Brooks, B. R.; Pastor, R. W. Langevin dynamics of peptides: the frictional dependence of isomerization rates of N-acetylalanyl-N'-methylamide. *Biopolymers* **1992**, *32*, 523−535.

(87) Darden, T.; York, D.; Pedersen, L. Particle mesh Ewald: An N log(N) method for Ewald sums in large systems. *J. Chem. Phys.* **1993**, *98*, 10089−10092.

(88) Essmann, U.; Perera, L.; Berkowitz, M. L.; Darden, T.; Lee, H.; Pedersen, L. G. A smooth particle mesh Ewald method. *J. Chem. Phys.* **1995**, *103*, 8577−8593.

(89) Ryckaert, J. P.; Ciccotti, G.; Berendsen, H. J. C. Numerical Integration of the Cartesian Equations of Motion of a System with Constraints: Molecular Dynamics of n-Alkanes. *J. Comput. Phys.* **1977**, *23*, 327−341.

(90) Raymond, J. W.; Willett, P. Maximum common subgraph isomorphism algorithms for the matching of chemical structures. *J. Comput.-Aided Mol. Des.* **2002**, *16*, 521−533.

(91) Shirts, M. R.; Chodera, J. D. Statistically optimal analysis of samples from multiple equilibrium states. *J. Chem. Phys.* **2008**, *129*, 124105.

(92) Press, W. H.; Teukolsky, S. A.; Vetterling, W. T.; Flannery, W. P. *Numerical Recipes in Fortran*, 2nd ed.; Cambridge University Press: Cambridge, 1992.

(93) Abramowitz, M. *Handbook of Mathematical Functions, With Formulas, Graphs, and Mathematical Tables*; Dover Publications, Inc.: USA, 1974.

(94) Kirkwood, J. G. Statistical mechanics of fluid mixtures. *J. Chem. Phys.* **1935**, *3*, 300−313.

(95) Straatsma, T. P.; Berendsen, H. J. Free energy of ionic hydration: Analysis of a thermodynamic integration technique to evaluate free energy differences by molecular dynamics simulations. *J. Chem. Phys.* **1988**, *89*, 5876−5886.

(96) Roe, D. R.; Bergonzo, C.; Cheatham, T. E. Evaluation of enhanced sampling provided by accelerated molecular dynamics with Hamiltonian replica exchange methods. *J. Phys. Chem. B* **2014**, *118*, 3543−3552.

(97) Syed, S.; Bouchard-Côté, A.; Deligiannidis, G.; Doucet, A. Non-reversible parallel tempering: A scalable highly parallel MCMC scheme. *J. R. Stat. Soc. Series B Stat. Methodol* **2022**, *84*, 321.

(98) Stanzione, D.; West, J.; Evans, R. T.; Minyard, T.; Ghattas, O.; Panda, D. K. *PEARC'20: Practice and Experience in Advanced Research Computing; Frontera: The Evolution of Leadership Computing at the National Science Foundation*; Association for Computing Machinery, 2020; pp 106−111.

(99) Boerner, T. J.; Deems, S.; Furlani, T. R.; Knuth, S. L.; Towns, J. In *PEARC'23: Practice and Experience in Advanced Research Computing*; Romanella, R. S. A., Knuth, S., Hackworth, K., Pummill, J., Eds.; ACCESS: Advancing Innovation: NSF's Advanced Cyberinfrastructure Coordination Ecosystem: Services & Supports; Association for Computing Machinery, 2023; pp 173−176.